

Towards realistic electronic structure calculations of strongly correlated electron systems

V. S. Oudovenko

Bogoliubov Laboratory for Theoretical Physics, Joint Institute for Nuclear Research, 141980 Dubna, Russia and
Center for Materials Theory, Department of Physics and Astronomy, Rutgers University, Piscataway, NJ 08854

G. Palsson, K. Haule, and G. Kotliar

Center for Materials Theory, Department of Physics and Astronomy, Rutgers University, Piscataway, NJ 08854

S. Y. Savrasov

Department of Physics, New Jersey Institute of Technology, Newark, NJ 07102
(Dated: April 14, 2024)

We review some aspects of the realistic implementation of the dynamical mean-field method. We extend the techniques introduced in Ref. 1 to include the calculations of transport coefficients. The approach is illustrated on $\text{La}_{1-x}\text{Sr}_x\text{TiO}_3$ material undergoing a density driven Mott transition.

I. INTRODUCTION

In recent years understanding of the physics of strongly correlated materials has undergone tremendous increase. This is in part due to the advances in the theoretical treatments of correlations, such as the development of dynamical mean-field theory (DMFT)¹. The great allure of DMFT is the flexibility of the method and its adaptability to different systems as well as the simple conceptual picture it allows us to form of the dynamics of the system. The mean-field nature of the method and the fact that the solution maps onto an impurity model, many of which have been thoroughly studied in the past, means that a great body of previous work can be brought to bear on the solution of models of correlated lattice electrons. This is exemplified by the great many numerical methods that can be employed to solve the DMFT equations.

DMFT has been very successful in understanding the mechanism of the Mott transition in model Hamiltonians. We now understand that the various concentration induced phase transitions can be viewed as bifurcation of a single functional of the Weiss field. The phase diagram of the one-band Hubbard model, demonstrating that there is a first order Mott transition at finite temperatures is fully established¹. Furthermore Landau like analysis demonstrates that all the qualitative features are quite generic at high temperatures². However the low-temperature ordered phases, and the quantitative aspects of the spectra of specific materials clearly require realistic treatment.

This triggered realistic development of DMFT in the last decade which has now reached the stage that we can start tackling real materials from an almost *ab initio* approach^{3,4}, something which in the past have been exclusively in the domain of density functional theories. We are now starting to see the merger of DMFT and such *ab initio* techniques and consequently the opportunities for doing real electronic structure calculations for strongly correlated materials which so far were not within

the reach of traditional density functional theories.

Density functional theory (DFT)⁵ is canonical example of *ab initio* approach, very successful in predicting ground state properties of many systems which are less correlated, for example the elemental metals and semiconductors. However it fails in more correlated materials. It is unable to predict that any system is a Mott insulator in the absence of magnetic order. It is also not able to describe correctly strongly correlated metallic state. As a matter of principle DFT is a theory of ground state or thermodynamic properties at finite temperatures. It's Kohn-Sham spectra cannot be rigorously identified with the excitation spectra of the system. In weakly correlated substances the Kohn-Sham spectra is a good approximation to start a perturbative treatment of the one-electron spectra using the GW method⁶. However this approach breaks down in strongly correlated situations, because it is unable to produce Hubbard bands. In orbitally ordered situations the LDA+U method⁷ produces the Hubbard bands, however this method fails to produce quasiparticle bands and hence it is unable to describe strongly correlated metals. Furthermore, once long range order is lost the LDA+U method reduces to LDA and hence it becomes inappropriate even for Mott insulators.

Dynamical mean-field theory is the simplest theory that is able to describe on the same footing total energies and the spectra of correlated electrons even when it contains both quasiparticle and Hubbard bands. Combined with LDA, one then has a theory which reduces to a successful method (LDA) in the weak correlations limit. In the static limit, one can show⁸ that LDA+U can be viewed as a static limit of LDA+DMFT used in conjunction with the Hartree-Fock approximation. Therefore LDA+U is equivalent to LDA+DMFT+ further approximations which are the only justified in static ordered situations. Up to now, the realistic LDA band structure was considered with DMFT for purpose of computing one-electron (photoemission) spectra and total energies.

Following Refs. 1,3,4 in this paper we extend this approach to computation of transport properties. Many

transport studies within DMFT applied to model Hamiltonians have been carried out, and the strengths (non-perturbative character) and limitations (absence of vertex corrections) are well understood. However applications to real materials require realistic computations of current matrix elements.

There are two ways in which DMFT can be used to understand the physics of real materials. The simplest approach, outlined in Ref. 1,3 is closely tied to the idea of model Hamiltonians. This requires i) methodology for deriving of the hopping parameters and the interaction constants ii) a technique for solving the dynamical mean-field equations and iii) an algorithm for evaluating the transport function which enters in the equations of transport coefficients. The second direction is more ambitious and focus on an integration of i) and ii) using functional formulations⁹.

In this paper we review the first approach. The emphasis here is in illustration of different aspects of the modeling which affect the final answer. This is necessary to obtain a balanced approach towards materials calculations. There are now many impurity solvers, they differ in their accuracy and computational cost. In the present paper we use two impurity solvers the Hirsch-Fye Quantum Monte Carlo (QMC) method¹⁰ and symmetrized nite-UNCA method (SUNCA)¹¹ comparing them in the context of simplified models without the additional complications of real materials. Instead we use the SUNCA method as an impurity solver to compute the transport properties and new developments using $\text{La}_{1-x}\text{Sr}_x\text{TiO}_3$ as an example material¹². For other reviews of realistic implementations of DMFT and electronic structure see Ref. 13.

In the next section II we shortly review a basic dynamical mean-field theory concepts and their application to realistic structure calculations. As computation of transport parameters requires knowledge of the self-energy coming from DMFT calculations which is based on impurity solvers we present a short review of two impurity solvers used in the paper in section III. Theory of the transport calculations is given in section IV. Test system used for transport calculations, which is doped LaTiO_3 ceramics, and DMFT results are described in section V. Results of dc-transport calculations are presented in section VI. And finally we come to conclusion in homonymous section VII.

II. DYNAMICAL MEAN-FIELD THEORY

A. Realistic DMFT formalism

A central concept in electronic structure theory is the full model Hamiltonian. Conceptually, one starts from the full many body problem containing all electrons and then proceeds to eliminate some high-energy degrees of freedom. The result is a Hamiltonian containing only a few bands. The determination of the model Hamiltonian is a

difficult problem in itself, which has received a significant attention^{14,15,16,17,18,19,20}. The Kohn-Sham Hamiltonian is a good starting point for the kinetic part of the Hamiltonian and can be conveniently expressed in a basis of linear momentum orbitals (LMO's)²¹, which need not be orthogonal (see Appendix B)), as

$$H_{\text{LDA}} = \sum_{i,j;m} (t_{ij}^m + t_{ij}^{m'}) C_{im}^\dagger C_{jm} \quad (1)$$

where i,j are atomic site indexes, m is orbital one, and denotes spin.

It is well known that LDA severely underestimates strong electron interactions between localized d- and f-electrons because the exchange interaction is taken into account only approximately via the functional of electron density. To correct this situation, the LDA Hamiltonian can be supplemented with a Coulomb interaction term between electrons in the localized orbitals (here we will call them a heavy set of orbitals). The largest contribution comes from the Coulomb repulsion between electrons on the same lattice site that we will approximate by the interaction matrix U^i of the heavy shell (h) of atom i as

$$H_{\text{int}} = \frac{1}{2} \sum_{i,h} U_{m_1 m_2 m_1' m_2'}^i C_{m_1}^\dagger C_{m_2}^\dagger C_{m_2'} C_{m_1'} \quad (2)$$

where m are orbital and are spin indexes. In the diagonal density approximation electron-electron interaction matrix $U_{m_1 m_2 m_1' m_2'}^i$ can be represented using screened Coulomb and exchange vertexes as

$$U_{m m'}^i = U_C^i \delta_{m m'} \quad (3)$$

$$J_{m m'}^i = U_C^i \delta_{m m'}$$

which are expressed via Slater integrals $F^{(i)}$, $i = 0; 2; 4; 6$ in the standard manner²². The Slater integrals can be linked to the average intra-atomic repulsion U and exchange J obtained from, e.g., LSDA supercell procedures via $U = F^0$ and $J = (F^2 + F^4)/14$. The ratio F^2/F^4 is to a good accuracy a constant 0.625 for d-electrons. Using the Coulomb and exchange matrices we can rewrite the interaction term as

$$H_{\text{int}} = \frac{1}{2} \sum_{i,h} U_{m m'}^i n_{i m} n_{i m'} = \frac{1}{2} \sum_{i,h} U_{m m'}^i n_{i m} n_{i m'} + \frac{1}{2} \sum_{i,h} (U_{m m'}^i - J_{m m'}^i) n_{i m} n_{i m'} \quad (4)$$

where index $m = (m; \sigma)$ combines the orbital and spin indexes. This equation also provides definition of the interaction matrix U^i which will be used further in the paper.

The LDA Hamiltonian already contains a part of the local interaction which has to be subtracted to avoid the double counting. The full Hamiltonian is thus approximated by

$$H = H_{\text{LDA}} - H_{\text{dc}} + H_{\text{int}} = H^0 + H_{\text{int}}; \quad (5)$$

where H^0 is the one-particle part of the Hamiltonian and will play a role of the kinetic term within a DMFT approach. The double counting correction can not be rigorously derived within LDA+DMFT. Instead, it is commonly assumed to have a simple static Hartree-Fock form, just shifting the energies of the heavy set

$$H_{dc,m}; \phi_m^0(k) = \epsilon_m; \phi_m^0 E_{dc}; \quad (6)$$

Here, i is atomic index in the elementary unit cell. The simplest approximation commonly used for E_{dc} is^{3,7}

$$E_{dc} = U \left(n_h - \frac{1}{2} \right); \quad (7)$$

where $n_h = \sum_m n_m$ is the total number of electrons in the heavy shell (see Appendix B).

In the spirit of DMFT, the self-energy is assumed to be local, i.e. k -independent, and non-zero only in the block of heavy orbitals. Therefore it is convenient to partition the Hamiltonian and the Green's function into the light and heavy set (denoted by l and h , respectively) as

$$G(k;!) = (! +) \begin{pmatrix} O_{hh} & O_{hl} \\ O_{lh} & O_{ll} \end{pmatrix}_k \quad (8)$$

$$\begin{pmatrix} H_{hh}^0 & H_{hl}^0 \\ H_{lh}^0 & H_{ll}^0 \end{pmatrix}_k \begin{pmatrix} hh(!) & 0 \\ 0 & 0 \end{pmatrix}^{-1};$$

where $[[::]]^{-1}$ means matrix inversion, ϵ is the chemical potential and O is the overlap matrix (see Appendix A).

The main postulate of the Dynamical Mean-Field Theory (DMFT)¹ formalism is that the self-energy is local, i.e. it does not depend on momentum, $\Sigma(k;!) = \Sigma(!)$. This postulate can be shown to be exact in the limit of infinite dimensions provided that the hopping parameters between different sites are scaled appropriately. Within this approach, the original lattice problem can be mapped onto an Anderson impurity model where the local Green's function and the self-energy, G_{loc} and Σ , are identified with the corresponding functions for the impurity model, i.e.

$$\Sigma_{imp}(!) = \Sigma(!) \quad \text{and} \quad G_{imp}(!) = G_{loc}(!); \quad (9)$$

Equations (9) along with the trivial identity

$$G_{loc}(!) = \sum_k G(k;!); \quad (10)$$

constitute a closed set of self-consistent equations. The only thing that remains is to solve the Anderson impurity model.

Notice that statement that the self-energy is diagonal is the basis dependent statement and if $\Sigma(!, n)$ is momentum independent in one basis and U_k is a unitary transformation from one basis to another, and LMTO Hamiltonian, H_{LDA} in the new basis is given by $U_k H_{LDA} U_k^\dagger$, then the self-energy in the new basis $\Sigma^0 = U_k \Sigma(!, n) U_k^\dagger$ is momentum dependent. Therefore DMFT approximation, if at all valid, is valid in one basis²³. Hence, we will

work in a very localized basis where the DMFT approximation is most justified.

In DMFT we construct the self-energy, Σ , as a solution of an Anderson impurity model with a non-interacting propagator (Weiss function) G_0

$$\Sigma_{imp} = \sum_{i,j} c_i^\dagger (!) G_0^{-1} (!; i) c_j (!) \quad (11)$$

$$+ \sum_{i,j} \frac{U}{2} n_i (!) n_j (!);$$

where i and j are running over indexes m . The Weiss function can be linked to the lattice quantities through the local Green's function and self-energy being are related to each other by the Dyson equation

$$G_{loc}(!, n)^{-1} = G_0(!, n)^{-1} - \Sigma(!, n); \quad (12)$$

Combining Eq. (8), (10) and (12) we finally obtain

$$G_0^{-1}(!, n) = \sum_k \frac{1}{(!, n +) O_k H_k^0 (!, n)} + \Sigma(!, n); \quad (13)$$

One can solve a very general impurity model defined by the action (11) and Weiss field (13). But it is much cheaper to eliminate the light (weakly interacting) bands and define an effective action in the subspace of heavy bands only. In this way, the local problem can be substantially simplified.

1. Downfolding

When a group of bands is well separated from the others it is clear that a reduced description of the problem is possible. In the one-electron approach it goes under the name downfolding²⁴. There are several prescriptions to carry out this procedure in the context of DMFT. Perhaps, the simplest approach is to reduce the Hamiltonian ($H^0 + H_{int}$) (see Eqs. (2), (1)) to the one having Hubbard like form for the bands in question. To estimate the hopping elements one can perform a tight-binding fit. The value of U to be used is then reduced, since ones computed in the constrained density functional calculations, it is screened by the bands which have been eliminated. After this procedure we arrive to a Hubbard Hamiltonian with a small number of bands

$$H = \sum_{i,j,m} t_{ij}^{m0} c_{im}^\dagger c_{jm} + H_{int};$$

where i, j run over lattice sites and $m; m^0 (!; i)$ label the orbital (spin) indices of the heavy set of orbitals.

We can also perform the downfolding at the level of DMFT. The starting point is Eq. (8) which is used to get the heavy block Green's function

$$G_{hh}(!) = \sum_k \begin{pmatrix} M_{hh}^k & M_{hl}^k M_{ll}^k \\ M_{lh}^k & M_{hh}^k \end{pmatrix}^{-1}; \quad (14)$$

where the quantity M^k is defined as

$$M^k = (I + \gamma) O(k) H^0(k); \quad (15)$$

here γ is a double index which is combination of h and l .

The low-energy form of Eq. (14) can be found by expanding around zero frequency and to linear accuracy in ω we obtain

$$G_{hh}(\omega) = \sum_k \frac{h}{Z_k} \frac{1}{\omega - E(k)} \frac{1}{h_h}; \quad (16)$$

where renormalization amplitude Z_k and effective Hamiltonian are given by

$$\begin{aligned} Z_k^{-1} &= O_{hh} + K_{hl} K_{ll}^{-1} O_{ll} K_{ll}^{-1} K_{lh} \\ &\quad O_{hl} K_{ll}^{-1} K_{lh} \quad K_{hl} K_{ll}^{-1} O_{lh}; \\ E(k) &= H_{hh}^0 \quad K_{hl} K_{ll}^{-1} K_{lh}; \\ K &= H^0 \quad O; \end{aligned} \quad (17)$$

Further, we can choose a new base in the heavy block such that the local Green's function has the usual form. First we define the average renormalization amplitude

$$Z = \sum_k Z_k; \quad (18)$$

and choose the transformation matrix such that

$$S^\gamma Z^{-1} S = 1; \quad (19)$$

The new overlap matrix and effective Hamiltonian become

$$O_{eff}(k) = S^\gamma Z_k^{-1} S; \quad (20)$$

$$H_{eff}(k) = S^\gamma E(k) S + O_{eff}(k); \quad (21)$$

$$= S^\gamma H_{hh} S; \quad (22)$$

and finally the local Green's function in the new base takes the form

$$G_{hh} = \sum_k [(I + \gamma) O_{eff}(k) H_{eff}(k)]^{-1}; \quad (23)$$

with the Dyson equation

$$G_{hh}^{-1} = G_{0hh}^{-1}; \quad (24)$$

and corresponding Weiss function defined as

$$G_{0hh} = [(I + \gamma)]^{-1}; \quad (25)$$

where hybridization function γ regularly behaves at infinity.

The selfenergy of the reduced model (23) is local, therefore the DMFT treatment is applicable. In this case, only the heavy bands need to be considered in calculation which greatly simplifies the complexity of the problem.

The reduced model, however, has in general more complicated Coulomb interaction matrix than we chose in

the original model. If we assume, that the diagonal components of Z are much larger than the off-diagonal, we obtain the same simple Hubbard-type interaction term within reduced model for the heavy block. The Coulomb interaction is however screened by the light bands and is reduced to

$$U \rightarrow U - Z^{-1} Z; \quad (26)$$

We can estimate the magnitude of the reduction of Coulomb repulsion by evaluating the above quantity explicitly. In the case the original base is orthogonal, i.e. $O = 1$, we get

$$\frac{U}{U} = \frac{1}{N} \text{Tr} H_{hl}^0 \frac{1}{H_{ll}^0} H_{lh}^0; \quad (27)$$

where N is the number of heavy bands.

In the case when the reduced model corresponding to Eq. (23) is degenerate and the basis is orthogonal (the overlap matrix $O_{eff}(k)$ is equal to unity) the self-energy and local Green's function are also degenerate and diagonal. Then the momentum sum in Eq. (23) can be replaced by the integral over energy and the local Green's function can be calculated using the standard Hilbert transformation

$$G(i!_n) = \int_{-1}^{Z+1} d\epsilon \frac{D(\epsilon)}{i!_n + \epsilon}; \quad (28)$$

Here, the density of states $D(\epsilon)$ is the density of states of the kinetic part of the reduced model $H_{eff}(k)$ in Eq. (23).

Other groups have used for $D(\epsilon)$ rescaled partial DOS as discussed in Appendix B. Possibility to use the Hilbert transformation substantially simplifies the calculation procedure and brings a number of conceptual simplifications¹³.

2. Upfolding

Upfolding is a procedure which is "inverse" to the downfolding one. One needs to use Eq. (22) to transform the self-energy obtained from DMFT calculations, Σ_{hh} , to the one, Σ_{hh} , which is inserted to the original LDA Hamiltonian in order to compute the local Green's function $(GF) G(i!_n)$. The local GF with upfolded self-energy reads

$$G(i!_n) = \sum_k \frac{1}{i!_n + \epsilon_k} \begin{pmatrix} O_{hh} & O_{hl} \\ O_{lh} & O_{ll} \end{pmatrix}_k \begin{pmatrix} H_{hh} & H_{hl} \\ H_{lh} & H_{ll} \end{pmatrix}_k \begin{pmatrix} H_{dc} & 0 \\ 0 & 0 \end{pmatrix}_{(i!_n)}; \quad (29)$$

where ϵ_k is the LDA chemical potential and H_{dc} is the double counting term Eq. (6). Instead of using formula (7), we rather deduce the constant shift of the heavy set

of bands by equating the total number of electrons to the integral of the spectral function

$$A_c(\omega) = \frac{1}{\pi} \text{Im} \sum_k G(\mathbf{k}; \omega) c_k^\dagger c_k;$$

multiplied by the Fermi function.

3. Algorithm to solve DMFT equations

To close the set of DMFT equations, a method to solve the local problem is required. In the following, we will focus our attention on two impurity solvers: QMC and SUNCA. In section III, we will briefly review both methods while a detailed comparison between the results obtained by those two approaches is given in section V D. Below, we summarize basic steps in the DMFT self-consistent scheme that delivers the local self-energy – crucial quantity to calculate transport and optical properties of a solid.

We started the iteration by a guess for the Weiss field G_0^{-1} from which the local Green's function G_{loc} was calculated by one of the impurity solvers. The self-energy was then obtained by the use of the Dyson equation (24). Momentum summation over the Brillouin zone, Eq. (23), delivers a new guess for the local Green's function and through the Dyson equation also for the Weiss field G_0^{-1} . The iteration is continued until the convergence is found to the desired level. The scheme can be illustrated by the following flow-chart

$$G_0^{-1} \text{ IMP solver } G_{DE} \xrightarrow{\text{DMFT SCC}} G_0^{-1};$$

where "DE" stands for the Dyson equation (24) and "DMFT SCC" means the DMFT self-consistent condition Eq. (23) or (28).

The QMC impurity solver is defined in imaginary time, therefore the following additional Fourier transformations between imaginary time and Matsubara frequency points are necessary

$$G_0(i\omega) \xrightarrow{\text{IFT}} G_0(\omega) \xrightarrow{\text{QMC}} G(\omega) \xrightarrow{\text{FT}} G(i\omega);$$

Here FT and IFT are Fourier and inverse Fourier transformations, respectively. After the self-consistency is reached, the analytic continuation is required to obtain the real-frequency self-energy. This issue is addressed in section III C.

The SUNCA method is implemented on real frequency axis to avoid the ill-posed problem of analytic continuation. As an input, it requires the bath spectral function $A_c(\omega) = \frac{1}{\pi} \text{Im} G_0^{-1}(\omega)$ and delivers the local spectral function $A_d(\omega) = \frac{1}{\pi} \text{Im} G(\omega)$

$$A_c(\omega) \xrightarrow{\text{SUNCA}} A(\omega) \xrightarrow{\text{KK}} G(\omega);$$

The real part of the local Green's function is obtained by the use of the Kramers-Kronig relation (KK).

III. IMPURITY SOLVERS

Among many methods used to solve the impurity problem we chose the Quantum Monte Carlo method¹⁰ and symmetrized finite-UNCA method¹¹. In this section we briefly describe both of them.

A. The Quantum Monte Carlo method

There are well known advantages and disadvantages of the QMC method and our choice is spurred by the fact that despite being slower than other methods the QMC is well controlled, exact method. As an input the QMC procedure gets Weiss function $G_0(\omega)$ and as an output it produces Green's function $G(\omega)$. We remind reader major steps taken for the QMC procedure. Usually one starts with impurity effective action S

$$S_{\text{eff}} = \sum_0^Z \sum_{\sigma} d_{\sigma}^\dagger d_{\sigma} c^\dagger(\omega) G_0^{-1}(\omega; \omega_0) c(\omega_0) + \frac{1}{2} \sum_0^Z \sum_{\sigma} d_{\sigma}^\dagger U_{\sigma} n_{\sigma}(\omega) n_{\sigma}(\omega); \quad (30)$$

where c, c^\dagger operators are fermionic annihilation and creation operators of the lattice problem, $\omega = \text{im}; g$.

The first what we should do with the action (31) is to discretize it in imaginary time space with time step such that $\beta = L$, and L is the number of time intervals

$$S_{\text{eff}} = \sum_{\sigma} c^\dagger(\omega) G_0^{-1}(\omega; \omega_0) c(\omega_0) + \frac{1}{2} \sum_{\sigma} U_{\sigma} n_{\sigma}(\omega) n_{\sigma}(\omega); \quad (31)$$

The next step is to get rid of the interaction term U by substituting it by summation over Ising-like auxiliary fields. The decoupling procedure is called the Hubbard-Stratonovich transformation^{25,26}

$$\exp(-U \sum_{\sigma} n_{\sigma} n_{\sigma}) = \frac{1}{2} \int (n_{\sigma} + n_{\sigma_0}) g_{\sigma} = \quad (32)$$

$$\frac{1}{2} \sum_{\sigma} \int_{-\infty}^{\infty} \exp(-S_{\sigma}(n_{\sigma} + n_{\sigma_0}) g_{\sigma});$$

where $\cosh S_{\sigma} = \exp(-\frac{U}{2})$, $S_{\sigma}(n_{\sigma})$ are auxiliary Ising fields at each time slice.

In the one-band Anderson impurity model we have only one auxiliary Ising field $S(n_{\sigma}) = 1$ at each time slice, whereas in the multiorbital case number of auxiliary fields is equal to number of σ, σ_0 pairs, i.e. C_2 . Applying the Hubbard-Stratonovich transformation at each time slice we bring the action to the quadratic form with the partition function

$$Z = \text{Tr}_{\text{FS}} \int \prod_{\sigma} dG_{\sigma}^{-1} \det G_{\sigma}^{-1}; \quad (33)$$

where GF in terms of auxiliary fields G^{-1} reads as

$$G_{fS}^{-1}(\omega; \omega_0) = G_0^{-1}(\omega; \omega_0) e^V - (e^V - 1); \omega; \quad (34)$$

with interaction matrix

$$V = \sum_{\omega_0} S_{\omega_0}(\omega) \omega_0; \quad (35)$$

where

$$\begin{aligned} \omega_0 &= +1 \text{ for } \omega < 0 \\ \omega_0 &= -1 \text{ for } \omega > 0. \end{aligned}$$

Once the quadratic form is obtained one can apply Wick's theorem at each time slice and make the Gaussian integration by Grassmann variables to get the full interacting GF

$$G(\omega; \omega_0) = \frac{1}{Z} \text{Tr}_{fS} e^{-V} \det G_{fS}^{-1}(\omega; \omega_0); \quad (36)$$

To evaluate summation Eq. (36) one uses Monte Carlo stochastic sampling. The product of determinants is interpreted as the stochastic weight and auxiliary spin configurations are generated by a Markov process with probability proportional to their statistical weight. More rigorous derivation can be found elsewhere^{1,26}.

Since the QMC method produces results in complex time ($G(\tau_m)$) with $\tau_m = m \tau$, $m = 1::L$) and the DMFT self-consistency equations make use of the frequency dependent Green's functions and self-energies we must have an accurate method to compute Fourier transforms from the time to frequency domain. This is done by representing the functions in the time domain by a cubic splined functions which should go through original points with condition of continuous second derivatives imposed. Once we know cubic spline coefficients we can compute the Fourier transformation of the splined functions analytically (see Appendices C and D).

B. The SUNCA

In this section we briefly review the second method, used to solve the multi-orbital Anderson impurity model, called Symmetrized finite-U NCA method¹¹. The method is based on the self-consistent perturbation theory with respect to the hybridization strength between the effective bath and the local system and is therefore exact in the atomic limit. However, this method sums up an infinite class of skeleton diagrams and takes into account a subclass of singular vertex corrections that are necessary to obtain the correct dynamic low-energy Fermi-liquid scale¹¹ and correct position of the Abrikosov-Suhl resonance. The SUNCA approximation does not contain only non-crossing diagrams but rather all the three-point vertex corrections of ladder-type and

should not be confused with the usual finite-U non-crossing approximation.

The SUNCA approach presents the advantage to provide directly real frequencies one-particle Green's functions. Local quantities like densities of states can therefore be computed for any regime of parameters without having to perform analytical continuation. Furthermore, the SUNCA method can be applied to arbitrary multi-band degenerate Anderson impurity model with no additional numerical cost. This is an important advantage compared to some other methods like Quantum Monte Carlo or exact diagonalization. The method is especially relevant for systems with large orbital degeneracy such as systems with f-electrons.

The pathologies that severely limit the usefulness of the non-crossing approximation in the context of DMFT are greatly reduced with inclusion of ladder-type vertex corrections. Nevertheless, they do not completely remove the spurious peak that forms at temperatures substantially below the Kondo temperature. To overcome this shortcoming, we employed an approximate scheme to smoothly continue the solution down to zero temperature. This was possible because at the break-down temperature the solution of SUNCA equations shows an onset of the Fermi-liquid state. As we will show in the subsequent chapters by comparison with QMC, SUNCA gives correct quasiparticle renormalization amplitude Z and the real part of the self-energy at zero frequency approaches the Luttinger value. The imaginary part of the self-energy, however, has a narrow spurious deep on top of the parabola that is formed around zero frequency. To remove the deep, we matched the Fermi-liquid parabolic form for imaginary part of the self-energy in the small window of the deep such that it smoothly connected the intermediate frequency region where the parabola was formed. We numerically found that this SUNCA pathology is rapidly reduced with increasing the number of bands i.e. it is much less severe in the case of three-band model than in one-band case.

Next, we give some details of the auxiliary particle technique together with the definition of the SUNCA approximation. Within the auxiliary diagrammatic method, the local degrees of freedom can be represented by auxiliary particles. To each eigenstate of the local Hamiltonian $H_{loc} |j_i\rangle = E_n |j_i\rangle$ we assign an auxiliary operator a_n such that $|j_i\rangle = a_n^\dagger |vac\rangle$. A general Anderson impurity model can then be expressed by

$$H = \sum_n E_n a_n^\dagger a_n + \sum_{k,m} c_{k,m}^\dagger c_{k,m} + \sum_{k,m,n} (V_{k,m} F_{n,m}^\dagger a_n^\dagger a_n c_{k,m} + h.c.); \quad (37)$$

where $F_{n,m}^\dagger = \ln j c_m^\dagger j^\dagger$, c_m^\dagger is a creation operator for the local electron and $c_{k,m}^\dagger$ creates an electron in the bath and m stands for the spin and band index. In order that electrons are faithfully represented by the auxiliary particles, two conditions must be satisfied:

- (i) An auxiliary particle a_n must be boson (fermion) if the state $|i\rangle$ contains even (odd) number of electrons.
- (ii) The local charge $Q = \sum_n a_n^\dagger a_n$ must be equal to one at all times $Q = 1$ expressing the completeness relation for the local states $\sum_n |i\rangle\langle i| = 1$.

The first condition merely request some care that has to be taken in evaluating diagrams while the second constraint, projection onto the physical Hilbert space, is somewhat more involved but can still be done exactly. The term Q can be added to the Hamiltonian and the limit $\beta \rightarrow 1$ has to be taken after the analytic continuation to the real frequency axes is performed. Taking this limit, actually leads to a substantial simplification of the analytic continuation. Namely, when evaluating self-energies for the pseudo-particles, only the integrals around the branch-cuts of the bath electron Green's function have to be considered while the integrals around the auxiliary particle Green's functions vanish by the projection.

The physical local Green's function (electron Green's function in $Q = 1$ subspace) can eventually be calculated with the help of the Abrikosov trick²⁷ which states that the average of any local operator that vanishes in the $Q = 0$ subspace is proportional to the grand-canonical (all Q values allowed) average of the same operator

$$\langle a_i \rangle_Q = 1 = \lim_{\beta \rightarrow 1} \frac{\langle a_i \rangle_Q}{\langle 1 \rangle_Q} : \quad (38)$$

By realizing that the local Green's function is proportional to the bath electron T-matrix, we have

$$G_{loc} = \lim_{\beta \rightarrow 1} \frac{1}{V^2 \langle 1 \rangle_Q} c; \quad (39)$$

where c is the bath electron self-energy calculated in the grand-canonical ensemble.

In the case of degenerate Anderson impurity model, an important simplification occurs in the Hamiltonian Eq. (37). Namely, pseudo-particles, corresponding to the states with the same number of electrons on the impurity site, are degenerate with energies $E_M = M + U/2$ ($M = 1, 2$), and pseudo Green's functions

$$G_M(i!) = 1/(i! - E_M - M(i!)); \quad (40)$$

where M is the number of electrons on the impurity. In the case of Anderson impurity model with $N=2$ bands, we need to consider only $N+1$ different propagators instead of dealing with 2^N pseudo-particles. Furthermore, if U is large and we are interested in doping levels not too far from an integer filling with M electrons, i.e. close to the Mott-insulating state, it is reasonable to assume that only fluctuations between local states with $M-1$, M and $M+1$ electrons on the impurity need to be considered. The single particle spectra will thus consist of lower Hubbard band, upper Hubbard band and a quasi-particle resonance while we ignore other Hubbard bands that are even more far away from the chemical potential.

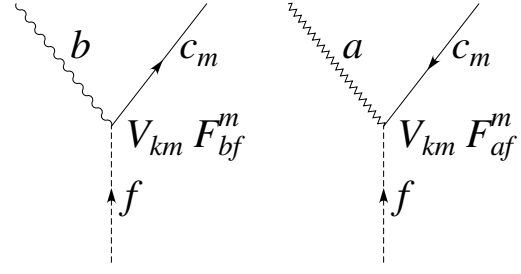


FIG. 1: The two bare vertices considered in the case of degenerate Anderson impurity model. Throughout this paper, conduction-electron c propagator is represented by solid line, while wiggly, dashed and zigzag lines correspond to the pseudo-particles with $M-1$, M and $M+1$ electrons on the impurity, respectively.

For example, in the case the filling is less than 1.5 we take into account empty state, singly occupied and doubly occupied states on the impurity while the triple occupancy is neglected. This is equivalent to adding to the original Hamiltonian an infinite three-particle interaction.

In the following, we will use letter b to denote the auxiliary particles with $M-1$ electrons on the impurity, f for M and a for $M+1$ electrons on the local level, respectively. In Fig. 1 we show the two bare three-point vertices that are left to us in the case of degenerate Anderson impurity model when considering those three types of states. Note that pseudo-particle b is $\binom{N}{M-1}$ degenerated, f is $\binom{N}{M}$ and a is $\binom{N}{M+1}$ degenerated, respectively. In case M is odd (even), particles a and b are bosons (fermions) while f are fermions (bosons).

The SUNCA approximation is a conserving approximation defined by a Luttinger-Ward type functional from which all self-energies are obtained as a functional derivatives, $\Sigma_a = \frac{\delta \Phi}{\delta G_a}$. The building blocks of Φ are dressed Green's functions of pseudo-particles G_b (depicted as a wiggly line), G_f (dashed line), G_a (zigzag line) and bath electron G_c (solid line). Due to the exact projection, only pseudo-particles are fully dressed while bath electron Green's function is not dressed.

The choice of diagrams was motivated by the Schrieffer-Wolff transformation showing that both fluctuations from M to $M-1$ and M to $M+1$ have to be considered totally symmetrically. In the case of one-band model we have for the exchange coupling $J = J_1 + J_2 = V^2 (\frac{1}{U} + \frac{1}{U})$. The exact Kondo temperature is proportional to $\exp(-J) = \exp(-(J_1 + J_2))$. It is well known that if one takes into account only non-crossing diagrams, the Kondo scale of the resulting approximation steeply drops with decreasing U and is of the order of $\exp(-J_1 - J_2)$ which can be orders of magnitude wrong. This happens because the simultaneous fluctuations between all three types of pseudo-particles are neglected. As was shown in Ref. 11, one needs to sum up an

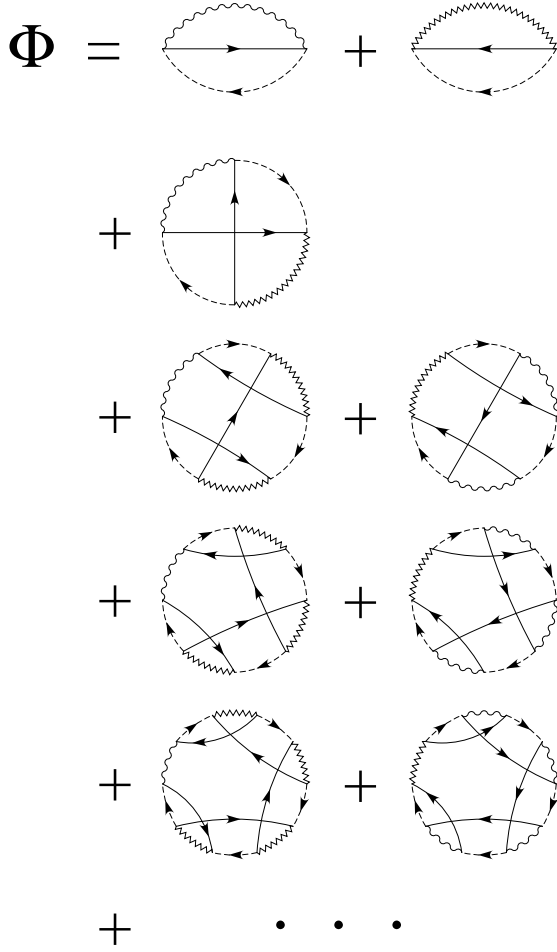


FIG. 2: Diagrammatic representation of the SUNCA generating functional to describe the degenerate Anderson impurity model.

infinite number of skeleton diagrams (SUNCA diagrams) to recover the correct exchange coupling consisting of two terms J_1 and J_2 , generated from the two types of vertices depicted in Fig. 1.

The SUNCA Luttinger-Ward functional, shown in Fig. 2, consists, in addition to NCA contributions (first two diagrams), of the diagrams where two conduction electron lines cross only once and the rest of the electron lines cross twice. Diagrams not included in SUNCA have higher order crossings. The lowest order neglected are of CTMA-type^{28,29} where all conduction electrons cross exactly twice. Note that due to the projection, any contribution to the Luttinger-Ward functional consists of a single ring of pseudo-particles since at any moment in time there must be exactly one pseudo-particle in the system.

The SUNCA selfenergies, obtained by differentiating the Luttinger-Ward functional, are shown in Fig. 3. The part of the pseudo-particle ring, where conduction electrons cross exactly twice, can be rewritten in the ladder type T-matrix. The additional two conduction lines, that

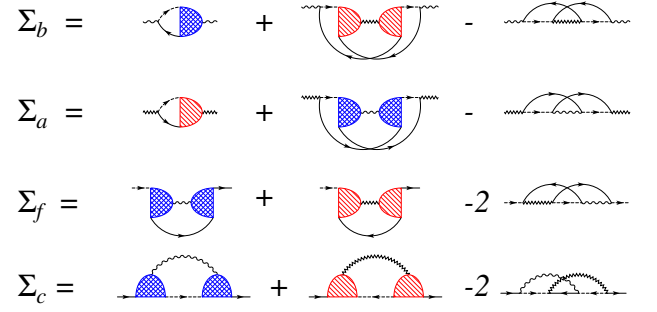


FIG. 3: Diagrammatic representation of the selfenergies, derived from SUNCA Luttinger-Ward functional (Fig. 4) in terms of the renormalized hybridization vertices, defined in Fig. 4. In each line the third diagram is subtracted in order to avoid double counting of terms within the first two diagrams.

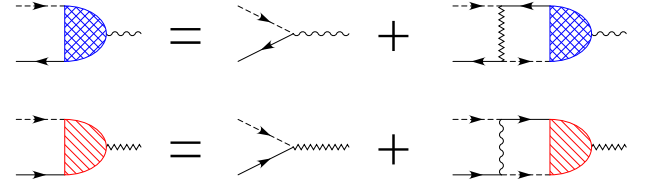


FIG. 4: Diagrammatic representation of the Bethe-Salpeter equations for ladder-type three-point vertex function.

cross only once, enable us to close T-matrix and convert it into three-point vertex shown in Fig. 4. This is important from practical point of view since the three-point vertex is numerically much more tractable than the full four-point vertex.

The expressions for the selfenergies defined by Fig. 3 and Fig. 4, together with the definitions of the Green's functions, Eq. (40), constitute a set of non-linear integral equations for Σ ; $\Sigma = a; b; f$. The local Green's function is calculated from the Eq. (39) using the self-consistently determined auxiliary propagators G . The SUNCA equations are given explicitly in Appendix E.

The SUNCA equations have been evaluated numerically by iteration. The two self-consistent loops, SUNCA and DMFT, can be merged together into one single set of equations. Starting with the initial guess for the bath spectral function A_c and pseudo-particle Green's functions G , the first guess to the T-matrix defined in Fig. 4 is determined. With this, the pseudo-particle selfenergies as well as the local Green's function may be deduced. From the DMFT self-consistent condition, the new bath spectral-function is calculated. With the updated pseudo-particle Green's functions and the new bath spectral-function one determines next approximation for the T-matrix, pseudo-particle selfenergies and local Green's function. The iteration is continued, until the convergence is found to the desired level.

C. Analytic continuation of the self-energy

The QMC simulation produces Green's function $G(\omega)$ of imaginary time $\omega = i\omega$ or equivalently Green's function and the self-energy defined in Matsubara frequency points. However, real-frequency self-energy is needed to obtain transport quantities. The analytic continuation of QMC data is required, which is an ill-posed problem and altogether hopeless if the precision of data is not extremely good and if the statistical errors are not taken into account properly. As is well known, Padé method is not very useful for analytic continuation of noisy QMC data. The maximum entropy method (MEM)³⁰ tries to overcome this problem by adding an entropy term to the functional to be minimized. This is one of the best methods present available and usually produces real-frequency Green's function of relatively high quality provided the data are carefully analyzed. We refer the reader to the original literature for the details³⁰.

However, the quasiparticle peak for realistic density of states can have quite rich structure since at low temperature it tries to reproduce the LDA bands around the Fermi-level, i.e., the spectral function approaches the LDA density of states contracted for the quasiparticle renormalization amplitude Z , $A(\omega) = Z\delta(\omega - \epsilon_F)$. The maximum entropy method has a tendency to smear out this rich structure because of the entropy term. At low temperature, this can lead to overshooting of spectral function and subsequently to the non-physical self-energy that ruins the causality. To avoid this pathology, we sometimes found useful to directly decompose the singular kernel with the Singular Value Decomposition (SVD). When constructing the real frequency data, we took into account only those singular values, which are larger than precision of the QMC data.

In imaginary time Green's $G(\tau)$ can be expressed by the spectral function as

$$G(\tau) = \int_{-\infty}^{\infty} d\omega f(\omega) e^{-\tau\omega} A(\omega); \quad (41)$$

or in discretized form

$$G = \sum_{\omega} f(\omega) e^{-\tau\omega} A_{\omega}; \quad A_{\omega} = \sum_{m=1}^M V_m S_m U_m^\dagger A_{\omega}; \quad (42)$$

where $U U^\dagger = 1$ and $V^\dagger V = 1$ are orthogonal matrices and S is diagonal matrix of singular values. The inversion is then simply given by

$$A_{\omega} = \sum_{m=1}^M U_m^\dagger \frac{1}{S_m} V_m G_{\omega}; \quad (43)$$

The magnitude of singular values drops very fast and only first few terms in the upper sum can be determined from the QMC data. The rest of the information, that determines mostly higher frequency points, can be acquired from the SUNCA spectral function. We therefore

approximated the sum in Eq. (43) by

$$A_{\omega} = \sum_{m=1}^M U_m^\dagger \frac{1}{S_m} V_m G_{\omega} + \sum_{m>M} U_m^\dagger \frac{1}{S_m} A_{\omega}^{\text{SUNCA}}; \quad (44)$$

where M can be determined by the precision of the QMC data, i.e., $V_m G_{\omega} > S_m$.

We plot the sum (44) in Fig. 5 where first 3, 6 or 9 coefficients were obtained from the QMC data. The corresponding smallest singular value is printed in the legend of the same figure. For comparison, we also display the spectral function obtained by the maximum entropy method and the SUNCA solution for the same parameters. The difference between the various curves gives as a rough estimate for the accuracy of the technique. As we see, the quasiparticle resonance is obtained by reasonably high accuracy, while the Hubbard band is determined with less accuracy. In the inset of Fig. 5 we plot the same curves in a broader window. As we see, the SVD does not guarantee the spectra to be positive at higher frequencies. This however does not prevent us to accurately determine most of the physical quantities.

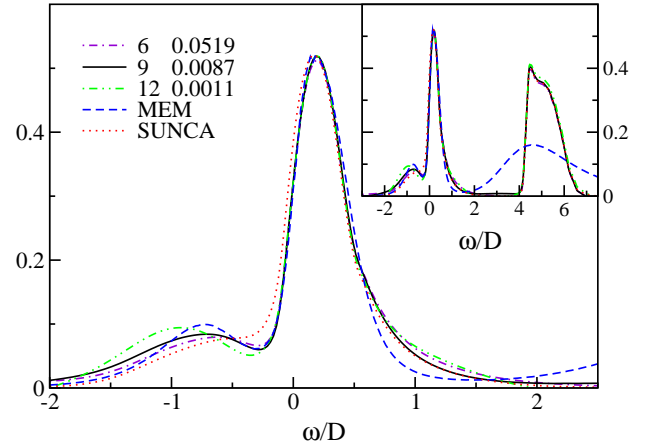


FIG. 5: Spectral function for semicircular DOS, inverse temperature $\beta = 16$ and density $n = 0.8$. Dot-dashed, full and double-dot-dashed curve correspond to the sum (44) with M chosen to be 6, 9 and 12, respectively. In legend, we also print the lowest singular value taken into account (S_M). For comparison we show maximum entropy spectra (dashed curve) and SUNCA spectra (dotted line). The inset shows the same spectra in a broader window.

Within DMFT, the real frequency self-energy can be obtained from the local Green's function by the inversion of the Hilbert transform. Although the implementation is very straightforward, we will briefly mention the algorithm we used. In the high-frequency regime, we can expand the Hilbert transform in terms of moments of the

DOS as

$$w(z) = \sum_{n=0}^{\infty} \frac{D^{(n)}(z)}{z^{n+1}} = \sum_{n=0}^{\infty} \frac{h^n i}{z^{n+1}}; \quad (45)$$

The series can be inverted and solved for z

$$z(w) = \frac{1}{w} + h^2 i + (h^4 i - h^2 i^2)w + (h^6 i - 3h^4 i h^2 i + 2h^2 i^3)w^2 + \dots; \quad (46)$$

For most of the frequency points, the expansion up to some higher power (w^8) gives already an accurate estimation for the inverse function. However, when w gets large, we need to use one of the standard root-finding methods to accurately determine the solution. This is however much easier than general root-finding in complex plane since we always have a good starting guess for the solution. We start evaluating the inverse function at high frequency where the absolute value of G is small and we can use the expansion in Eq. (46). Then we use the fact that Green's function is a continuous function of a real frequency and we can follow the solution from frequency point to frequency point by improving it with few steps of a secant (or Newton) method. A special attention, however, must be paid not to cross the branch-cut and get lost in the non-physical complex plane. Therefore, each secant or Newton step has to be shortened if necessary. The self-energy is finally expressed by the inverse of Hilbert transform w^{-1} as

$$= i + \frac{1}{w} G; \quad (47)$$

Fig. 6 shows the imaginary part of self-energy obtained by both analytic-continuation methods. As a reference and comparison we also show the results obtained by SUNCA method, which is defined and evaluated on real frequency axes and hence does not require analytic continuation. The low-frequency part of the self-energy is again very reliably determined and does not differ for more than 3%.

IV. TRANSPORT COMPUTATION

A. Transport theory

The transport parameters of the system are expressed in terms of so called kinetic coefficients, denoted here by A_m . The equation for the electrical resistivity, ρ , is given by

$$\rho = \frac{k_B T}{e^2} \frac{1}{A_0}; \quad (48)$$

and the thermopower, S , and the thermal conductivity, κ , are expressed through

$$S = \frac{k_B}{e} \frac{A_1}{A_0}; \quad \kappa = k_B \left(A_2 - \frac{A_1^2}{A_0} \right); \quad (49)$$

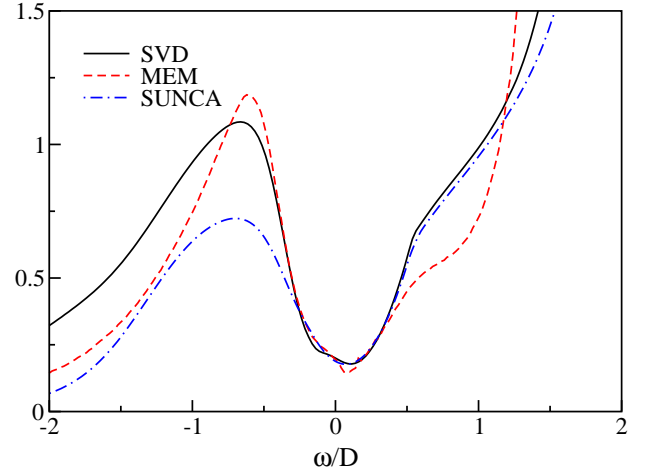


FIG. 6: Imaginary part of the self-energy obtained from the Green's function by the inverse of the Hilbert transform. Full-line was obtained by the Singular Value decomposition, dashed by the maximum entropy method and dot-dashed by SUNCA. Parameters used are the same as in Fig. 5

Within the Kubo formalism³¹ the kinetic coefficients are given in terms of equilibrium state current-current correlation functions of the particle and the heat currents in the system. Namely we have

$$A_m = \lim_{\eta \rightarrow 0} \text{Im} Z_m(i\eta + i0); \quad (50)$$

where

$$Z_0(i) = \frac{i\hbar}{i} \int_0^\infty dt e^{-i\hbar t} \langle j^x(t) j^x(0) \rangle; \quad (51)$$

$$Z_1(i) = \frac{i\hbar}{i} \int_0^\infty dt e^{-i\hbar t} \langle j^x(t) Q^x(0) \rangle; \quad (52)$$

$$Z_2(i) = \frac{i\hbar}{i} \int_0^\infty dt e^{-i\hbar t} \langle Q^x(t) Q^x(0) \rangle; \quad (53)$$

To evaluate these correlation functions, an expression for electric and heat currents, j^x and Q^x , are needed. Once those currents are evaluated, then calculation of the transport properties within DMFT reduces to the evaluation of the transport function

$$\chi^{\alpha\alpha}(\omega) = \frac{1}{V_C} \sum_k \text{Tr} f v_k^\alpha(\omega) \chi_k^\alpha(\omega) g; \quad (54)$$

and the transport coefficients

$$A_m = N_{\text{spin}} \frac{1}{h} \int_{-1}^1 d\omega \chi^{\alpha\alpha}(\omega) f(\omega) f(\omega + \mu); \quad (55)$$

The momentum integral in Eq. (54) extends over the Brillouin zone, V_C is the volume of the unit cell. The simplest form of the velocity is $\hbar \frac{1}{m} \mathbf{r}_x \cdot \mathbf{k} = v_k$ and it requires evaluation of matrix elements of \mathbf{r}_x . However an alternative form of the current and the transport

function can be derived via the Peirls substitution generally in the non-orthogonal basis and is described in Appendix F. These two procedures generally give different answers^{23,32,33}.

Next we define the energy dependent velocity as

$$\mathbf{v}_k(\epsilon) = \frac{1}{\hbar} \frac{\partial \epsilon_k(\epsilon)}{\partial \mathbf{k}} \quad (56)$$

The second term is due to the non-orthogonality of the basis or more speci cally due to overlap between orbitals at different sites, local non-orthogonality does not contribute to the velocity. The spectral density matrix $\rho_k(\epsilon)$ is the multiorbital generalization of the regular single orbital density of states and is given in terms of the retarded Green's function, G , of the system by the equation

$$\rho_k(\epsilon) = \frac{1}{2} [G_k(\epsilon) - G_k^*(\epsilon)] \quad (57)$$

Finally the Green's function is given by

$$G_k(z) = (z - \epsilon_k)^{-1} O_k H_k^0(z)^{-1} \quad (58)$$

Note here, that in accordance with the DMFT the self-energy matrix is assumed momentum independent. Now given an effective Hamiltonian for the system, an overlap matrix and the self-energy, the equations above give a complete prescription for computing the transport parameters. For computation of Eq. (54) we have developed two methods, one method generalizes the analytical tetrahedron method (ATM)³⁴ and the other one uses one-particle GF method in DMFT³, used to compute spectral densities in band structure calculations. First the total Hamiltonian, $H_k(\epsilon) = H_k^0 + \Sigma(\epsilon)$ is diagonalized and written in the form

$$H_k(\epsilon) = O_k A_k^R(\epsilon) E_k(\epsilon) A_k^L(\epsilon) O_k^\dagger \quad (59)$$

where E_k is the diagonal matrix of complex eigenvalues and A_k^R and A_k^L are the right and the left eigenvector matrices respectively. Then the Green's function can be written as

$$G_k(\epsilon) = A_k^R(\epsilon) [(z - \epsilon_k) I - E_k(\epsilon)]^{-1} A_k^L(\epsilon) \quad (60)$$

with I being the identity matrix. The transport function can now be expressed as

$$\chi^{\alpha\alpha}(\epsilon) = \frac{1}{2} \frac{1}{V_C} \text{Re} \sum_{k,p,q} \mathbf{r}_{k,pq}^{\alpha} \mathbf{r}_{k,pq}^{\alpha} D_{k,p} D_{k,q}^* \quad (61)$$

where the matrices \mathbf{r}^{α} , \mathbf{s}^{α} and \mathbf{t}^{α} are

$$\begin{aligned} \mathbf{r}_k^{\alpha} &= \mathbf{r}_k^{\alpha}(\epsilon) A_k^L(\epsilon) \mathbf{v}_k^{\alpha}(\epsilon) A_k^R(\epsilon); \\ \mathbf{s}_k^{\alpha} &= \mathbf{s}_k^{\alpha}(\epsilon) A_k^L(\epsilon) \mathbf{v}_k^{\alpha}(\epsilon) A_k^L(\epsilon); \\ \mathbf{t}_k^{\alpha} &= \mathbf{t}_k^{\alpha}(\epsilon) A_k^R(\epsilon) \mathbf{v}_k^{\alpha}(\epsilon) A_k^R(\epsilon); \end{aligned} \quad (62)$$

and D_k is a diagonal matrix defined by

$$D_k = D_k(\epsilon) [(z - \epsilon_k) I - E_k(\epsilon)]^{-1} \quad (63)$$

When the computation of the transport function is carried out one is faced with computing integrals of the form

$$\begin{aligned} \chi_k^{\alpha\alpha} &= \frac{\mathbf{r}_{k,pq}^{\alpha} \mathbf{r}_{k,qp}^{\alpha}}{(z - \epsilon_{k,p})(z - \epsilon_{k,q})}; \\ \chi_k^{\alpha\beta} &= \frac{\mathbf{s}_{k,pq}^{\alpha} \mathbf{t}_{k,qp}^{\beta}}{(z - \epsilon_{k,p})(z - \epsilon_{k,q})}; \end{aligned} \quad (64)$$

The strategy that is used to compute these integrals is similar in spirit to the analytical tetrahedron method. The Brillouin zone is split up into a collection of equal sized tetrahedra and the integral over each tetrahedron is taken using linear interpolation between the four corners of the tetrahedron. In the analytical tetrahedron method the numerator and the energy eigenvalues in the denominator are linearized independently and the resulting integral is then done analytically. In our case we would want to follow the same rule which results in two linear functions in the denominator. Unfortunately we have not been able to evaluate that integral in the most general case, i.e. when none of the tetrahedron corners are degenerate although solutions can be found for degenerate cases when at least two of the four corners of the tetrahedron are identical. Hence we have to pursue further approximations which we outline below.

The two main integrals that we need to compute are of the form

$$\begin{aligned} T_{SS}^{pq} &= \sum_{k \in \text{tet}} \frac{F(k)}{(z - \epsilon_{k,p})(z - \epsilon_{k,q})}; \\ T_{OS}^{pq} &= \sum_{k \in \text{tet}} \frac{F(k)}{(z - \epsilon_{k,p})(z - \epsilon_{k,q})}; \end{aligned} \quad (65)$$

Here tet denotes the tetrahedron and SS indicates that the imaginary parts of both denominators have the same sign and OS indicates that they have the opposite sign. This is ensured by the fact that the self-energy is retarded and z is real. For the diagonal case ($p = q$) the T_{SS} integral can be computed exactly by linearizing the eigenvalues in the denominator, one simply needs to differentiate the ATM formulas by Lambin and Vigneron³⁴. For the diagonal T_{OS} however we note that the numerator is real and therefore we can write the integral in the following form

$$T_{OS}^{pp} = \text{Im} \sum_{k \in \text{tet}} \frac{F(k)}{\epsilon_{k,p}} \frac{1}{z - \epsilon_{k,p}}; \quad (66)$$

where $\epsilon_{k,p} = \text{Im} \epsilon_{k,p}$. We note that $\epsilon_{k,p}$ is solely due to the self-energy, which is momentum independent and thus it is reasonable to expect that $\epsilon_{k,p}$ changes little with momentum. Hence the term in the parenthesis will be approximated linearly within the tetrahedron and the resulting integral can be computed with the ATM.

The off-diagonal case ($p \neq q$) for both T_{SS} and T_{OS} is treated the same way so we will just look at T_{SS} . Both

factors in the denominator are inspected and we determine which one has larger modulus (on average if necessary). Then we write the integral on the form

$$T_{SS}^{pq} = \sum_{k_2} \frac{F(k)}{(z - E_k)_L} \frac{1}{(z - E_k)_S}; \quad (67)$$

where L indicates the denominator with the larger modulus and S indicates the one with the smaller modulus. The term in the parenthesis is now approximated linearly within the tetrahedron and the resulting integral can be computed with the ATM.

The approach described here to compute the transport function has been tested numerically against models where other methods can be used to evaluate the transport function. For cubic systems with nearest neighbor hopping one can for instance evaluate both the density of states and the transport function quite efficiently using Fast Fourier Transform¹. In general the results are quite accurate.

B. Small scattering limit

In order to make connections with previous approaches to the computation of transport properties it is interesting to consider the small scattering limit. So we take the self-energy of the form

$$\Sigma(k) = \Sigma^0(k) + \Sigma^1(k); \quad (68)$$

where $\Sigma^0(k)$ is the real part of the self-energy matrix, $\Sigma^1(k)$ is the imaginary part and Σ^1 is a small parameter.

It is clear that the transport function will diverge as $\Sigma^1 \rightarrow 0$ and thus we can approximate the numerator matrix elements to zeroth order in Σ^1 . Within this approximation the transport function can be written as

$$\Sigma^{xx}(k) = \frac{1}{V_C} \sum_{k,p} (v_{k,p}^x)^2 \frac{1}{(z - E_{k,p})} \left(1 + \frac{\Sigma^0(k)}{E_{k,p}} \right); \quad (69)$$

where $E_{k,p}^0$ are the eigenvalues of $H_k + \Sigma^0(k)$ and $v_{k,p}^x$ denotes the corresponding band velocity. The lifetime $\tau_{k,p}(k)$ is formally given by

$$\tau_{k,p}(k) = \frac{1}{2 \text{Im} E_{k,p}}; \quad (70)$$

here $E_{k,p}$ are the eigenvalues of the full Hamiltonian. The imaginary part of these eigenvalues is due to the scattering term and is therefore to first approximation linear in Σ^1 . The lifetime therefore diverges as $\Sigma^1 \rightarrow 0$ but for a finite value of Σ^1 we regard Eq. (69) as an approximation to the transport function and we will refer to this approach as the small scattering approximation.

In spite of the limited validity of the small scattering approximation it is useful in the sense that it is computationally much simpler to evaluate the transport function in the small scattering approximation than in the general

case. Therefore it can be used in order to obtain a rough idea of the behavior of the transport parameters.

The equations of the small scattering approximation are very similar to the formulae that have been used by other groups to compute the transport parameters of real materials^{35,36,37}. In particular the assumption of constant lifetime is quite often used in practice, especially when the thermopower is being calculated. In this case we obtain

$$\Sigma^{xx}(k) = \Sigma^{xx}(k); \quad (71)$$

where the so called transport density, ρ , is defined as

$$\Sigma^{xx}(k) = \frac{1}{V_C} \sum_{k,p} (v_{k,p}^x)^2 \left(1 + \frac{E_{k,p}^0}{E_{k,p}} \right); \quad (72)$$

Numerical tests have shown that while the small scattering approximation can be quite good for broad bands it does not work well in narrow bands such as the dynamically generated quasiparticle bands of strongly correlated systems due to constant time approximation used.

In the case of the thermopower we obtain

$$S = \frac{k_B}{e} \frac{R_1}{R_1} \frac{\Sigma^{xx}(k) f'(k) f(k)}{\Sigma^{xx}(k) f(k) f(k)} \quad (73)$$

$$T \rightarrow 0 \quad \frac{k_B}{e} \frac{2k_B T}{3} \frac{d}{d} \ln \Sigma^{xx}(k) : \quad (73)$$

This of course is the classical Mott relation for the thermopower. In the literature this equation is often quoted with the transport density replaced by the spectral density and much emphasis placed on the fact that in case the Fermi-level coincides with a Van Hove singularity the thermopower diverges. This conclusion is not supported when the correct form for the thermopower is used since no Van Hove singularities are present in the transport density.

For free electrons the transport density is given by

$$\Sigma^{xx}(k) = \frac{1}{12} \frac{2m_e}{h^2} \frac{3}{2} \frac{3}{2}; \quad (74)$$

and therefore we get

$$S = \frac{k_B}{e} \frac{2k_B T}{2} \frac{1}{F} = n^{-2/3} T \quad 0.281 \frac{nV}{K}; \quad (75)$$

where the density, n , is measured in electrons per cubic Bohr radius and the temperature, T , is measured in Kelvin. In case the effective mass of the electrons is enhanced the thermopower will simply increase by the enhancement factor.

The enhancement of the thermopower can also be deduced from the Mott equation in case the only effect of the real part of the self-energy is to change the effective mass of the bands that cross the Fermi-surface. If we assume that the change in effective mass is the same for

all the bands that participate in the transport the low-temperature thermopower becomes

$$S = \frac{k_B}{e} \frac{2k_B T}{3Z} \frac{d}{d\epsilon} \ln \rho_{xx}(\epsilon_0); \quad (76)$$

where the non-interacting transport density $\rho_{xx}(\epsilon)$ is defined by

$$\rho_{xx}(\epsilon) = \frac{1}{V_C} \sum_{\mathbf{k}, p}^X (v_{\mathbf{k}, p}^{0,xx})^2 (\epsilon - E_{\mathbf{k}, p}^0): \quad (77)$$

Here Z denotes the quasiparticle residue of the bands involved. Hence we see indeed that the low-temperature thermopower is enhanced by a factor of $1=Z$ compared to the non-interacting thermopower.

To summarize theoretical part of the paper we provide the computational scheme used to obtain the transport properties

$$\text{LDA} \xrightarrow{\text{H L}} \text{DMFT} \xrightarrow{\text{H LDA}} \text{TRANSPORT};$$

i.e.

run LDA program to obtain the Kohn-Sham (LDA) Hamiltonian

make tight-binding calculations (or downfolding) to extract kinetic part of the effective Hamiltonian

construct the Hubbard-like effective Hamiltonian adding the Coulomb repulsion to the kinetic part of the effective Hamiltonian

run DMFT-QMC (SUNCA) solver to obtain the self-energy for the effective Hamiltonian

construct LDA+DMFT Hamiltonian upfolding the self-energy to the LDA Hamiltonian

run transport program with the LDA+DMFT Hamiltonian.

V. TEST SYSTEM AND DMFT RESULTS

A. Test System

To test obtained transport equations on a realistic system we decided to use doped $\text{La}_{1-x}\text{Sr}_x\text{TiO}_3$ compound. The $\text{La}_{1-x}\text{Sr}_x\text{TiO}_3$ series has been studied very extensively in the past^{38,39,40,41,42,43} and can be regarded as being one of the prime examples exhibiting the Mott-Hubbard metal-insulator transition. The end compound LaTiO_3 when prepared well is a Mott-Hubbard insulator although in the literature it is often characterized as a correlated or a poor metal. At high temperature this material is paramagnetic. The other end compound SrTiO_3 is an uncorrelated band insulator with a direct gap of 3.3 eV. Electronic structure properties of the

$\text{La}_{1-x}\text{Sr}_x\text{TiO}_3$ series is governed by the triple degenerate cubic t_{2g} bands of the 3d orbitals (d^1 ionic configuration)⁴⁴. In the distorted structure of LaTiO_3 the degeneracy of the band has been lifted and the single electron occupies a very narrow, non-degenerate d_{xy} band⁴⁵. Studies of the magnetic susceptibility do indeed indicate that the electronic structure of the Pbnm phase is that of a narrow d_{xy} band, which then with doping changes into a broad t_{2g} band (calculated bandwidth is $W = 2.7$ eV) with degenerate d_{xy} , d_{xz} and d_{yz} orbitals in the Ibm and Pm3m phases. As a function of doping the material behaves as a canonical doped Mott insulator. The specific heat and the susceptibility are enhanced, the Hall number is unrenormalized while the photoemission spectral function has a resonance with a weight that decreases as one approaches half filling. Very near half filling, (for dopings less than 8 %) the physics is fairly complicated. At small doping an antiferromagnetic metallic phase is observed^{42,46,47}.

To obtain LDA band structure of LaTiO_3 we used the linear muffin-tin orbitals (LMTO) method in its atomic sphere approximation (ASA) with the basis $\text{Ti}(4s;4p;3d)$, $\text{O}(2s;2p)$ and $\text{La}(6s;5p;5d)$ assuming for simplicity instead a real orthorhombic structure with a small distortions a cubic one with the same volume and the lattice constant $a_0 = 7.40$ a.u.. This approximation brings to a slight overestimation of the effective bandwidth and underestimation of the band gap between valence and conduction bands. In photoemission studies of LaTiO_3 ¹² similar basis has been used.

Using LDA band structure one can compute and compare with experiment the linear coefficient of specific heat which is simply given in terms of the density of states at the Fermi level by

$$= 2.357 \frac{mJ}{m\text{olK}^2} \frac{\rho_{\text{tot}}(E_F) [\text{states}/(\text{eV unit cell})]}{Z}; \quad (78)$$

where Z is the quasiparticle residue or the inverse of the mass renormalization. In LDA calculations the value of Z is equal to one. Doping dependence of the linear coefficient of specific heat in LDA calculations was computed within the rigid band model. Our results along with the experimental data are presented in Table I.

In general, we see that the LDA data for γ are lower than the experimental values, indicating a strong mass renormalization. We note also that as we get closer to the Mott-Hubbard transition the effective mass grows significantly. What is consistent with DMFT modeling of the Mott-Hubbard transition which shows that indeed the effective mass diverges at the transition. We should note however that this is not a necessary signature for the Mott-Hubbard transition: in V_2O_3 the pressure driven metal-insulator transition is accompanied by the divergence of the effective mass whereas the doping driven transition in the same system does not show that divergence⁴⁹.

The physical picture of the studied material is quite

Doping	Experiment	LDA
5%	16.52	3.23
10%	11.51	3.16
20%	8.57	3.00
30%	7.70	2.82
40%	6.21	2.67
50%	5.38	2.52
60%	4.55	2.38
70%	4.35	2.19
80%	3.52	2.10

TABLE I: The linear coefficient of specific heat, γ , for $\text{La}_{1-x}\text{Sr}_x\text{TiO}_3$ measured in units of $\frac{\text{mJ}}{\text{mol K}^2}$. The experimental data is taken from ⁴⁸. LDA data for the linear coefficient of specific heat are computed from LaTiO_3 LDA DOS.

transparent, very near half filling (dopings less than 8 %) the Fermi energy becomes very small and now is comparable with the exchange interactions and structural distortion energies. A treatment beyond single site DMFT then becomes important to treat the spin degrees of freedom. On the other hand for moderate and large doping, the Kondo energy is the dominant energy and DMFT is expected to be accurate. This was substantiated by a series of papers which compared DMFT calculations in a single band or multiband Hubbard models using simplified density of states with the physical properties of real materials. Ref. 50 addressed the enhancement of the magnetic susceptibility and the specific heat as half filling is approached. The optical conductivity and the suppression of the charge degrees of freedom as the Mott insulator is approached was described in Refs. 51,52, the observation that the Hall coefficient is not renormalized was found in Refs. 53,54. Finally the thermoelectric power on model level using iterative perturbation theory (IPT) as in purity solver was investigated by Palsson et al.⁵⁵.

Given the fact that only very simple tight-binding parameterizations were used in those works, and the fact that a large number of experiments were in line with the same value of parameters one should regard the qualitative agreement with experiment as very satisfactory. The photoemission spectroscopy of this compound, as well as in other transition metal compounds are not completely consistent with the bulk data, and it has been argued that disorder, and modeling of the specific surface environment is required to improve the agreement with experiment ⁵⁶. In this situation, it is clear that this is the simplest system for study, and it was in fact the first system studied by LDA+DMFT ³.

The important questions to be addressed are the degree of quantitative accuracy of DMFT. Furthermore, given the simplicity of this system, and the existence of well controlled experiments, it is an ideal system for testing the effects of different approximations within the LDA+DMFT scheme.

B. The model

As we pointed out in Sec. II for a correct description of a system with strong electron correlations one needs to bring the self-energy into the heavy orbitals. For this purpose a model which correctly describes the physics of interacting orbitals is needed. In this paper we consider a three-band Hubbard model which underlying non-interacting dispersion relation is that of the degenerate cubic t_{2g} band of the transition metal 3d orbitals. For simplicity the Hubbard interaction term is taken to be SU(6) invariant i.e. there is equal interaction between two electrons of opposite spin in the same orbital as there is between two electrons in different orbitals on the same site. The more general case will be revisited in future publications.

Value of the interaction strength in our model is chosen large enough to exhibit metal-insulator behavior in the studied compound. In units of half bandwidth, D , the interaction strength is taken to be equal $U = 5D$. The interaction strength should be regarded as an input parameter which value has been adjusted to the experimental situation. Saying this, we mean the chosen interaction strengths should be good enough to reproduce as many physical properties as only possible with maximum proximity to experiment. To investigate dependence of calculated physical properties on the interaction strength we calculate all properties studied in this paper for two values of Coulomb repulsion $U = 3D$ and $5D$. On the model level $U = 4D$ is the value very close to the minimum interaction to get metal-insulator transition (MIT) for integer filling $n = 1$ even in three-fold degenerate Hubbard model using DMFT as an instrument which takes care of the interaction in the system. Hence our choice of the interaction should guarantee exploration of two physically different behaviours of the system with and without the MIT. In literature absolute value of Coulomb interaction is magnitude under discussion mainly because there is no direct and reliable method to extract it neither experimentally nor theoretically. The uncertainty between different theoretical methods^{12,57} attempted to estimate value of U is quite substantial ranging the interaction strength from 3.2 eV to 5 eV.

It should be noticed that although this choice of parameters is consistent with insulating behavior of this system it might have limited validity in the real system at low doping. Since $\text{La}_{1-x}\text{Sr}_x\text{TiO}_3$ is known to undergo several structural transformations upon doping and in particular the structure of LaTiO_3 is distorted away from the cubic perovskite structure and in fact the distortion lifts the degeneracy of the t_{2g} orbitals and the groundstate orbital is a narrow non-degenerate d_{xy} orbital. Hence one might expect that the Mott-Hubbard transition in this system would be better described in a one-band model ($x < 0.08$). At larger dopings ($x > 0.08$) it is however clear that the system is degenerate and thus our model can be expected to give a reasonably good description in the larger doping range. In the present paper

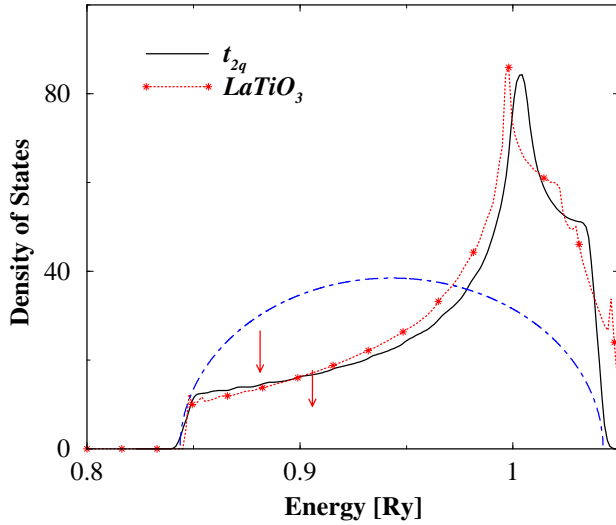


FIG. 7: LDA DOS of LaTiO_3 (dotted line with star symbols), its tight-binding t_{2g} (solid line) and semicircular DOS (dot-dashed line). Arrows indicate Fermi level position for filling $n = 0.8$ (the first one is for the semicircular DOS, and the second one is for the tight-binding t_{2g}).

we do not consider the effect of lifting the degeneracy due to Jahn-Teller distortion rather we explore the three-fold degenerate Hubbard model in the whole region of doping interval including $n = 1$ point.

The kinetic part of the model Hamiltonian has been obtained from tight-binding LMTO ASA calculations. The band structure of the compound around the Fermi level consists of three-fold degenerate $\text{Ti } 3d_{t_{2g}}$ band, hosting one-electron, which is a rather well separated from an empty $\text{Ti } 3d_{e_g}$ band located above t_{2g} band. A rather broad gap below t_{2g} separates $\text{Ti } 3d$ and completely filled $2p$ oxygen band. Hence it is quite straightforward to make the tight-binding t_{2g} band to be used in the impurity solvers. To achieve asymmetry in tight-binding DOS one needs take into account the next nearest neighbors, so called, t^0 term on Ti sublattice. The dispersion which we obtained from the t is the following: $\epsilon_k = 2t(\cos k_x + \cos k_y) + 2t^0 \cos(k_x + k_y) + 2t_z \cos k_z$, where $t = 0.02424$, $t^0 = 0.006$, $t_z = 0.00151$ in Ry units. t_{2g} part of LaTiO_3 DOS (dotted line) and its t (solid line) are presented in Fig. 7. We also added one more curve in Fig. 7 corresponding to semicircular DOS which we will use for different kind of benchmarking of our approach.

Making tight-binding t_{2g} of $\text{Ti } 3d_{t_{2g}}$ bands in LaTiO_3 we effectively do downfolding of the whole Hamiltonian (better to say the main part of the Hamiltonian without $\text{Ti } 3d_{t_{2g}}$ bands) of the compound onto three t_{2g} bands i.e. we incorporate information of the whole Hamiltonian into part of it. In this case H_{eff} and O_{eff} are 3×3 matrices. H_{hh} and O_{hh} are parts of the Hamiltonian and the overlap matrix corresponding to t_{2g} block of the original Hamiltonian. H_{ll} and O_{ll} are parts of the Hamiltonian

and the overlap matrices of the Hamiltonian without t_{2g} block.

Our results of downfolding are presented in Fig. 8. We plotted bands of the whole Hamiltonian which correspond to $\text{Ti } 3d_{t_{2g}}$ bands by solid lines (the upper line is double degenerate one) and bands obtained from Eq. (21) by dashed lines. We see that bandwidth of t_{2g} bands ob-

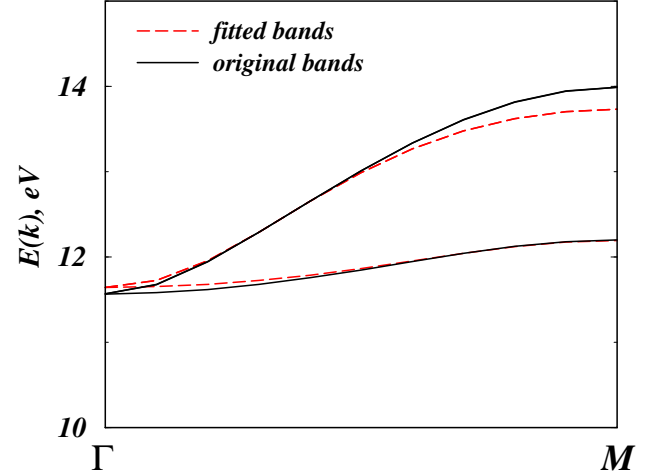


FIG. 8: t_{2g} bands of real band structure of LaTiO_3 (solid lines) and downfolded bands obtained from Eq. (21). The Fermi level is at $E_F = 12.54$ eV.

tained from Eqs. (21) is only slightly smaller than the original one. The downfolding reproduces original band structure one-to-one in approximately 1 eV energy window around the chemical potential. If one uses only H_{hh} and O_{hh} matrices (not effective H_{eff} and O_{eff} but simply parts of the total Hamiltonian corresponding to t_{2g} block) one gets nearly dispersionless levels only as it is naturally expected.

As the last step in this section we calculate the transport function and the thermoelectrical power for three-fold degenerate tight-binding model. The transport function that we obtain for this model is shown in Fig. 9. We note that the slope of the transport function in the hole doping (< 0.0) regime is positive and therefore the LDA evaluation of the thermopower results in electron-like thermopower. The results for a few chosen doping values computed at temperature equal to 300 K are displayed in table II where we have also displayed the experimental results from Ref. 43.

It is quite noteworthy that for the two lowest doping values in the table the LDA and the experiment are in a good agreement. For higher values of doping however the experimental values are about twice as large as the LDA values. The good agreement at low doping should be regarded as mostly accidental one since the experimental data for doping values less than 5% show the hole-like thermopower which the LDA of course will not be able to reproduce.

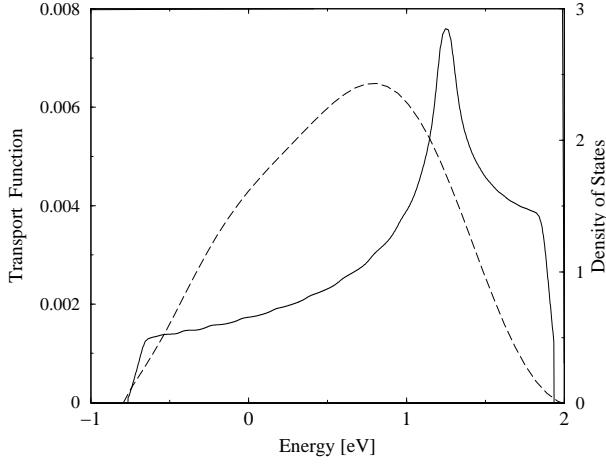


FIG. 9: The transport function for the LDA tight-binding Hamiltonian computed within the small scattering approximation with a constant lifetime for all orbitals along with DOS for $n = 0.8$. Zero energy corresponds to the zero temperature Fermi-level.

Doping	Experiment	LDA data
5%	-5.2	-5.6
25%	-9.3	-7.8
50%	-18.3	-9.3
75%	-29.4	-18.2
80%	-41.2	-22.8

TABLE II: The thermopower, S , of $\text{La}_{1-x}\text{Sr}_x\text{TiO}_3$ at 300K measured in units of V/K is computed using LDA band structure. The experimental data are taken from ⁴³.

C. Summary of DMFT results

In the previous section we described how to obtain the Hubbard like Hamiltonian with kinetic part coming from downfolded bands and interaction part defined by renormalized Coulomb repulsion. In this section we address the issue how to compute and what is the main effect of the second part of the Hamiltonian, namely interactions, on physical properties of the studied system. The method which we used to solve the Hamiltonian is the dynamical mean-field theory which we described in section II.

Strong correlations dramatically renormalize tight-binding LDA DOS which we plot in Fig. 10 by dashed line. As it is seen from the plot it has bandwidth $2D$ and very asymmetric shape. In the same figure it is shown by solid line the renormalized DOS obtained from DMFT-QMC calculations at temperature $T = 980 \text{ K}$. Instead one QP peak of the non-interacting t_{2g} DOS we have nearly classical Hubbard DOS picture where the central peak of the non-renormalized DOS is redistributed between two Hubbard subbands and strongly renormalized central peak. Although the total bandwidth increases

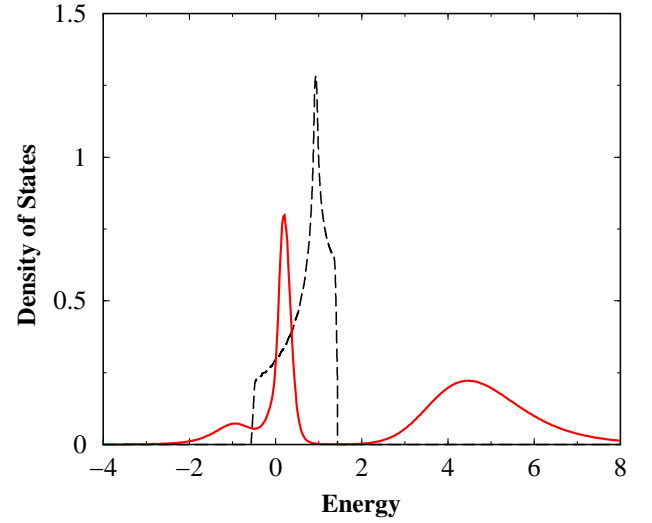


FIG. 10: Tight-binding (dashed lines) and renormalized (solid line) DOSes for filling $n=0.8$ and $\beta = 32$ at $U = 5D$.

substantially, width of the central peak gets strongly reduced. We also notice the steepness of renormalized DOS at the chemical potential indicating reduction of the quasiparticle residue which is in LDA equal to one.

So, the main effect expected from electron interactions is to reproduce the Mott transition when the system approaches an integer filling. One can see indications of the MIT in filling, n , dependencies of the chemical potential, μ , and quasiparticle residue, Z . The MIT is clearly indicated by jump of μ versus n dependence (the chemical potential changes while filling remains the same) plotted in Fig. 11 and also by vanishing energy scale seen in Z versus n dependence in Fig. 12 while approaching the Mott transition.

In Fig. 11 we plot the chemical potential against filling around $n = 1$ for three values of Coulomb interaction $U = 3D; 4D$ and $5D$ in units of the half bandwidth and for two shapes of DOS (semicircular and tight-binding). We notice here that both semicircular and realistic DOS are renormalized in such a way that they run in interval $[-D; D]$ with norm equal to one. First two upper curves presented in Fig. 11 correspond to $U = 3D$. The upper curve obtained using tight-binding DOS and lower one comes from semicircular DOS. The first curve is nearly a straight line crossing $n = 1$ point while the line corresponding to semicircular DOS is about to make a jump which is clearly presented in the behaviour of $U = 4D$ line. The jump becomes even more pronounced for $U = 5D$ and both, semicircular and tight-binding, DOSes. Let us notice that absolute value of the jump for tight-binding DOS is smaller than for semicircular DOS. From this figure one can easily conclude that the critical interaction when insulating behaviour appears in the system should be somewhere between $U = 3D$ and $U = 4D$ closer to the second value (the final conclusion about the insulating behaviour one can make from energy depen-

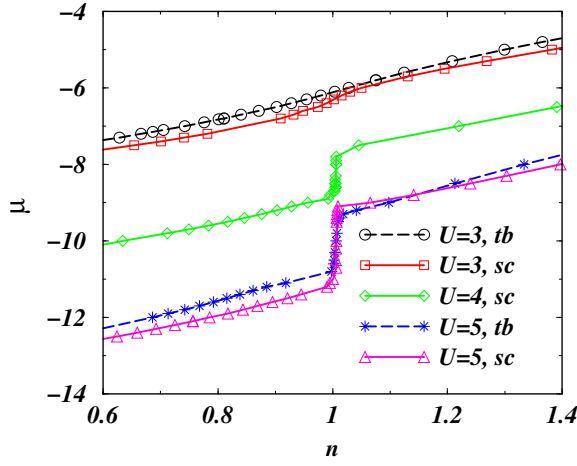


FIG. 11: The chemical potential, μ , versus filling, n for semi-circular (sc) and tight-binding (tb) DOSes and various values of interaction, U , and temperature $T = 16$.

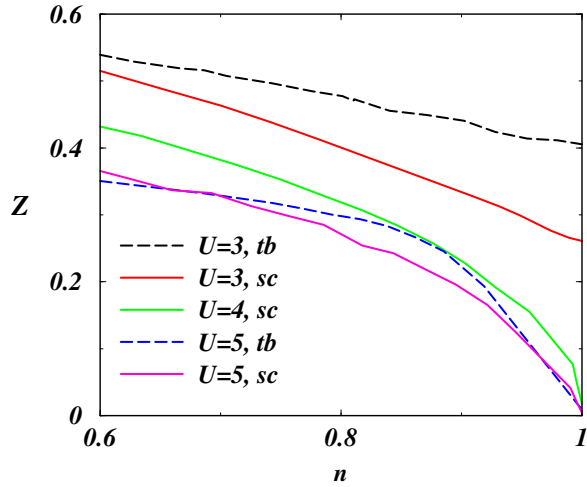


FIG. 12: Density dependence of the quasiparticle residue, Z , for semi-circular (sc) and tight-binding (tb) DOSes and various values of interaction, U and temperature $T = 16$.

dence of DOS on real axis).

Similar to the Z against n dependence the MIT behaviour one can observe from the doping dependence of the quasiparticle residue which is presented in Fig. 12. In Fig. 12 we plot five curves for the same values of interaction and shapes of DOSes as in the previous graph. As we expected for $U = 3$ (both DOSes) and $n = 1$ we have a finite value of Z . Notice that again (as in the previous plot) tight-binding DOS shows more metallic behaviour (larger value of Z and more straight line than in the case of semi-circular DOS). All other values of the interaction clearly show insulating behaviour of the system.

So, now when one can see how electron correlations change physical behaviour of the system, we remind that the main input to DMFT-QMC or DMFT-SUNCA pro-

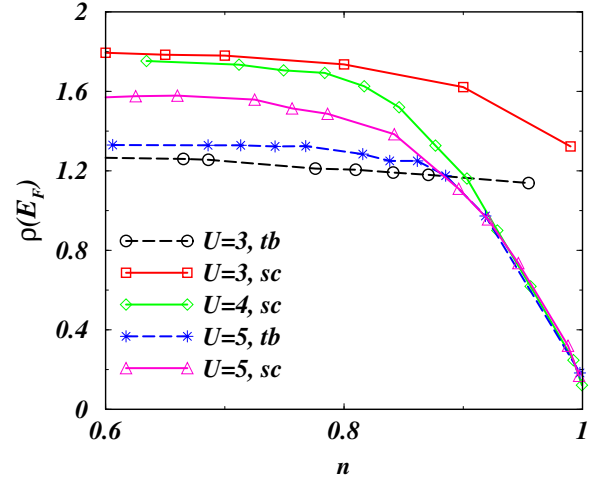


FIG. 13: DOS at the Fermi level, $\rho(E_F)$ [states=(eV unit cell)], vs filling, n , for semi-circular (sc) and tight-binding (tb) DOSes and various values of interaction, U . All of the data was computed for $T = 16$.

cedure consists from the shape of DOS (semi-circular or tight-binding) and the value of interaction, U . We will analyze both shapes of DOSes for two values of U mentioned above.

Using our results presented in Fig. 12 and behaviour of $\rho(E_F)$ presented in Fig. 13 we can calculate the linear coefficient of specific heat, γ . As we saw above, LDA results differ a lot from experimental values for γ . Now we want to know whether we can get any improvements applying DMFT, which changes the quasiparticle residue, Z , and renormalizes DOS.

In Fig. 14 we plot the linear coefficient of specific heat against filling for different values of Coulomb repulsion and semi-circular and tight-binding DOSes. We can notice that for the same repulsion strength the linear coefficient of specific heat for the semi-circular DOS is larger than for tight-binding DOS which follows from larger pinning value in the case of semi-circular DOS. Comparing U dependencies for the semi-circular DOSes we see that the linear coefficient of specific heat for $U = 3D$ is nearly linear function till filling $n = 1$ which one can explain by almost linear dependence of the quasiparticle residue. For $U = 4D$ and $U = 5D$ doping dependence of the linear coefficient of specific heat reproduces the experimental behaviour and the only question left is how close theoretical and experimental results are. From the plot we see that in general results the semi-circular DOSes are far from the experiment while for the tight-binding DOS the experimental curve just in between $U = 3D$ and $U = 5D$ lines. We can claim a rather good agreement (contrary to LDA situation) between DMFT and experimental curves for whole range of dopings. The divergence of the linear coefficient of specific heat shows the d-electron effective mass at the Fermi level is strongly enhanced on approaching the MIT⁴⁶. In the case of $U = 5D$ a small

"overshooting" of the linear coefficient of specific heat for large doping can be explained by 10-15 % inaccuracy in the procedure of the quasiparticle extraction (we define it from the self-energy on Matsubara axis), plus one can slightly tune the interaction strength, which probably should be something like $4.5 - 4.8D$. In general agreement between DMFT-QMC results and experimental one is quite good.

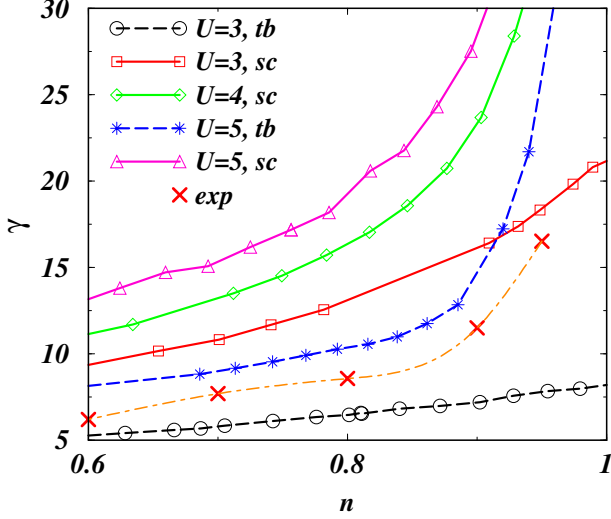


FIG. 14: The linear coefficient of specific heat, $[\text{mJ mol}^{-1} \text{K}^{-2}]$, vs. the density for different interaction strength and DOSes at temperature $T = 16$.

So we can summarize the linear coefficient of specific heat results saying that changes in the spectral weight, Z , are the main source of the improvement of our results for the linear coefficient of the specific heat. Those changes are most remarkable for $U = 5D$ where Z tends to zero while density approaches the integer filling $n = 1$. Diverging behaviour of linear coefficient of specific heat for small doping in the real material can be explained by one of the structural transitions happening in LaTiO_3 , at doping less than 5% the three-fold degeneracy is lifted and we effectively have only one-band model for which $U = 3D$ could be large enough to get the MIT transition at integer filling.

Besides the degeneracy and the structural transition, temperature belongs to major players on the field of the MIT. The energy scale which separates low and high temperatures is given by $D^0 = ZD$ where D is uncorrelated bandwidth of the system and Z is the quasiparticle residue. Since the metal-insulator transition is accompanied by the vanishing of the quasiparticle residue we see that in order to access the low-temperature phase we need to go to lower and lower temperatures as we get closer to integer filling. Hence we can not expect to be able to see clear evidence of the divergence of γ for the range of temperatures we are working in QMC approaching integer filling.

D. Comparison QMC and SUNCA

In this section we analyze and compare two impurity solvers i.e. QMC and SUNCA which have been described in section III. Below we present results of those two methods and choose one of them to compute transport. Similar to the case of LDA calculation, in calculation the impurity problem we also need to make a compromise between speed and accuracy. It is well known that QMC impurity solver is very expensive but exact (the only approximation used in QMC is the Trotter breakup) while SUNCA is cheap method but it is based on more approximations. QMC works in imaginary time and Matsubara frequency domain while SUNCA works on real frequency axis. To compute transport properties one needs the self-energy on real axis. In the case of QMC it is necessary to make the analytical continuation using maximum entropy or singular decomposition method to get the self-energy on real axis as it was described in section IIIC. This is the weakest point in the DMFT-QMC procedure. DMFT-SUNCA working on real axis has the self-energy immediately after the self-consistency is reached.

As we noticed in the previous subsection the main task of the interaction (read the impurity solver) is to produce the MIT at integer fillings. And one of the criteria of insulating behaviour in the system is vanishing quasiparticle weight. In Fig. 15 we compare the quasiparticle residue, Z obtained from DMFT-QMC and DMFT-SUNCA methods as function of doping for $U = 5D$ and realistic DOS. We see that both methods are in a good agreement with each other. We also provide Z versus n curve calculated using iterative perturbative theory⁵⁸ (IPT) to see that all three impurity solvers produce at least qualitatively the same trends.

Now we can go further and compare electron GF on Matsubara axis. Imaginary axis is a natural space of work for QMC and to compare results with SUNCA we used Lehmann representation connecting spectral function on real axis with GF on imaginary axis. The representation is analytical and exact, hence, the comparison can be made without any assumptions and approximations or uncertainties which could arise in the case of the analytical continuation.

In Fig. 16 we plot real and imaginary parts of GF on Matsubara axis for QMC (symbols) and SUNCA (lines) at different dopings and temperature $T = 2$ where one would expect very good agreement for the methods (as higher temperature as better and faster both methods work). And indeed it is the case for all the curves. In Fig. 17 we plot GF and imaginary parts of the self-energy for lower temperature, $T = 16$ (temperature which is mostly used in our calculations) and for 10 and 20 % of dopings (they are our usual dopings used in calculations).

As we can conclude from presented curves we have quite good agreement between the two methods and hence we can use SUNCA in our transport calculations where behaviour of the self-energy on real axis around

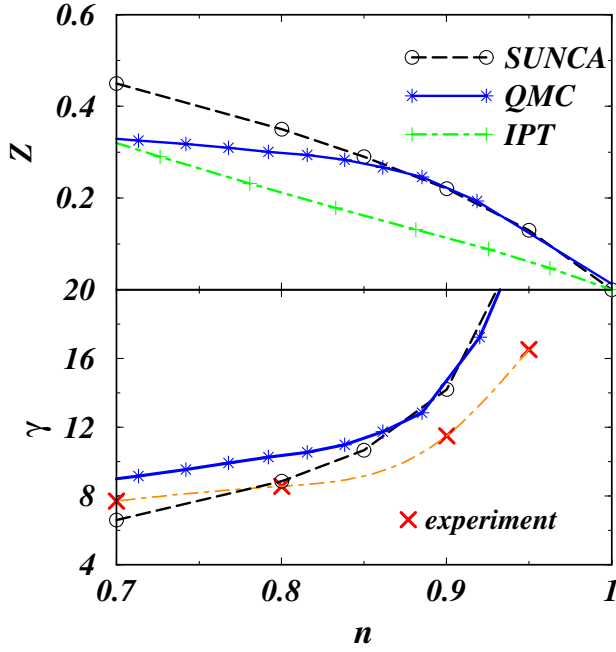


FIG. 15: Filling dependence of the quasiparticle residue, Z , and the linear coefficient of specific heat, γ , obtained from two impurity solvers: QMC (solid line with stars) and SUNCA (dashed line with circle symbols) for $U = 5D$, temperature $= 16$. Experimental points are given by cross symbols and dot-dashed line is used as a guide for eye. Tight-binding density of states was used in the self-consistency loop of the DMFT procedure. For comparison we also provide Z vs n curve obtained with IPT method for the same parameters as ones used in QMC and SUNCA calculations.

the Fermi level is very crucial for the transport properties which are extremely sensitive to the shape, slope and value of the self-energy at the Fermi level. Transport properties become more and more sensitive to all the details of the transport function at the Fermi energy with lowering temperature. Taking into account all the comparisons made and calculations done we conclude that SUNCA is fast and accurate enough method in comparison with QMC to compute the transport properties of the compound.

VI. RESULTS OF TRANSPORT CALCULATIONS

A. Spectral and transport functions in the real system

Before to do transport computations it is worth to study spectral and transport functions dependencies on doping and temperature. As we discussed in the previous section V D we will use SUNCA as main method to compute transport properties (one can avoid the analytical continuation procedure in this case). But, at any rate,

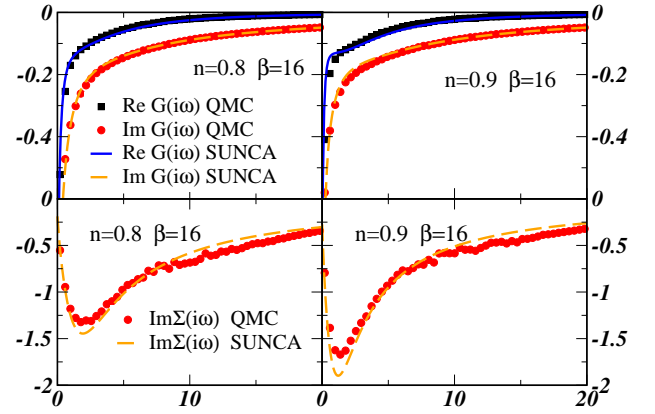


FIG. 16: Comparison of energy dependencies of imaginary and real parts of GF on Matsubara axis for different dopings computed using two impurity solvers: QMC (circles) and SUNCA (solid line) used in DMFT self-consistency procedure with semicircular DOS for $U = 5D$ and temperature $= 2$.

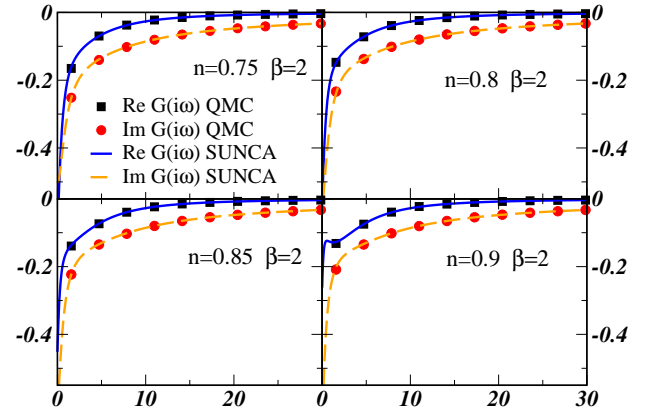


FIG. 17: In the two upper panels we compare energy dependencies of imaginary and real parts of GF on Matsubara axis for dopings $n = 0.8$ and 0.9 computed using QMC (circles) and SUNCA (solid line). In the low panels we plot imaginary parts of the self-energies for the same parameters as in the upper panels. We used semicircular DOS in DMFT self-consistency procedure and $U = 5D$ at temperature $= 16$.

we also did calculations with QMC impurity solver and compare results obtained from the two impurity solvers and describe differences between them when they are the most noticeable.

In Fig. 18 we plotted the density of states per spin (the lower Hubbard band and quasiparticle peak are shown in the main panel and the inset shows the whole energy range) at filling $n = 0.8$ for various values of temperature. Here temperature is measured in units of the half-bandwidth, $D = 1.35$ eV and thus the actual temperature range is quite large with the smallest temperature, corresponding to $T = 0.05D$, being around 780 K. The highest temperature plotted is equal to one but it is still not large enough to make incoherent motion in the system to be dominant. As we can see temperature changes are quite

substantial (the lower Hubbard band nearly disappeared and quasiparticle peak is shifted towards the upper Hubbard band, indicating tendency to join the upper Hubbard band and form incoherent broad bump) but they are still not enough to reach the incoherent motion state (the upper Hubbard band is changed but still it is very good separated from the QP peak { lower Hubbard band creation). This situation is the expected one as we know the QP picture disappears for temperature higher than Coulomb repulsion, U , which is 5D in our case. Hence, for $T = 5D$ one will see only incoherent motion in the system. Let us notice here the difference between SUNCA and QMC where in the last method the spectral density is just a single hump corresponding to purely incoherent carrier dynamics observed already for temperature

$\beta = 1$. If we start from incoherent picture and lowering temperature, then the incoherent hump splits up and the Hubbard bands start to form. For even lower temperature the lower Hubbard band moves completely below the Fermi-surface and the coherent quasiparticle peak appears at the Fermi-level. The lower Hubbard band starts to form at $\beta = 4$, QP peak is formed for $\beta = 10$. For temperature lower than $\beta = 16$ weight of the QP peak nearly does not change. We observe similar behaviour of DOS in SUNCA where the shape of the QP and the lower Hubbard band change only slightly for temperatures lower than $T = 0.1D$. Described discrepancies on real axis between the two methods are entirely in the domain of the analytical continuation which is maximum entropy method which reliably reproduces only low-energy part. One more interesting thing we should notice in Fig. 18 which is temperature dependence of DOS value at the Fermi level. When this value reaches the one of non-interacting DOS we say that the pinning condition is obeyed. The temperature when the pinning condition is reached is called the pinning temperature and it strongly depends on doping. For filling $n = 0.8$ as we can conclude

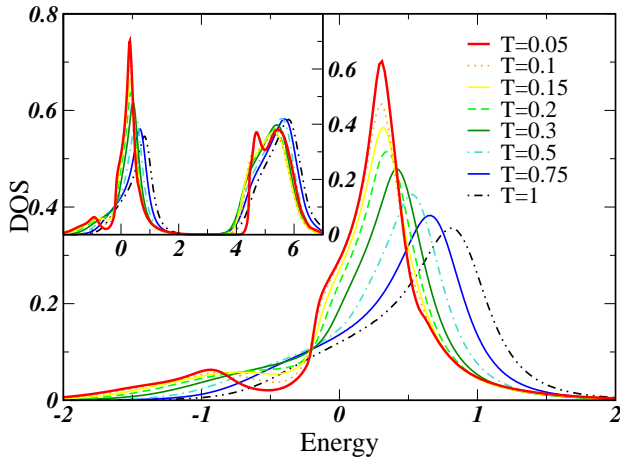


FIG. 18: Temperature dependence of DMFT density of states for $n = 0.8$ and $U = 5D$. Larger frequency interval is plotted in the insert. Energy is in units of halfbandwidth, D .

In Fig. 19 we plotted the density of states per spin for $T = 0.05$ and different values of doping. Choice of temperature was dictated by consideration that it should be lower than the pinning temperature for the largest filling presented. With doping growing the quasiparticle peak broadens and its spectral weight increases a lot while the weight of the lower Hubbard band changes a little (doping changes are 10-20%). All the weight, which the QP peak gained, came from the upper Hubbard band (see insert in Fig. 19 where larger energy interval is presented). With doping increasing the system becomes less and less correlated and in the limit of 100% doping Hubbard bands vanish and the quasiparticle peak transforms into free and empty tight-binding band. With doping decreasing the QP peak vanishes and the system becomes insulating for the repulsion $U = 5D$. As we mentioned it before, for three-band degenerate Hubbard model, $U = 3D$, which is often used in description of LaTiO_3 , is not enough to reproduce the insulating behaviour, which appears only for $U = 4.5 - 5D$.

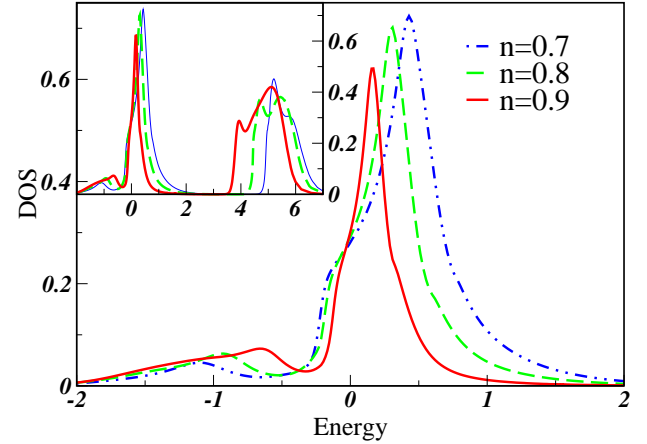


FIG. 19: Doping dependence of DMFT density of states for $T = 0.05$ and $U = 5D$. Larger frequency interval is plotted in the insert. Energy is in units of halfbandwidth, D .

In Figs. 20 and 21 we presented dependence of imaginary part (main panels) and real part (inserts) of the self-energy on temperature and doping for the same temperatures as in Figs. 20 and the same dopings as in Fig. 21. In Fig. 20 we see nice quadratic behavior of the self-energy for low temperatures with the minimum at around the chemical potential (zero in our case) which is then rises and shifts with the temperature to the right-hand side. Real part of the self-energy reflects the quasiparticle residue, Z , and with lowering the temperature the QP residue increases and approaches the pinning value. The doping dependence of the imaginary part of the self-energy shows that the self-energy at the chemical potential decreases with increasing of doping. This is exactly what one should expect for a system close to free-electron state where more quadratic and smaller imaginary part of the self-energy is anticipated. The real part of the self-energy shows the same tendency with in-

creasing doping as in the case of the temperature dependence: the curve which crosses the Fermi level becomes more at. At zero doping it should have zero derivative at the chemical potential signaling about $Z = 1$. The self-energy is extremely important characteristic of the system as it is the only quantity which enters into transport calculations. Using the self-energy one computes the transport functions which is main ingredient of all transport equations.

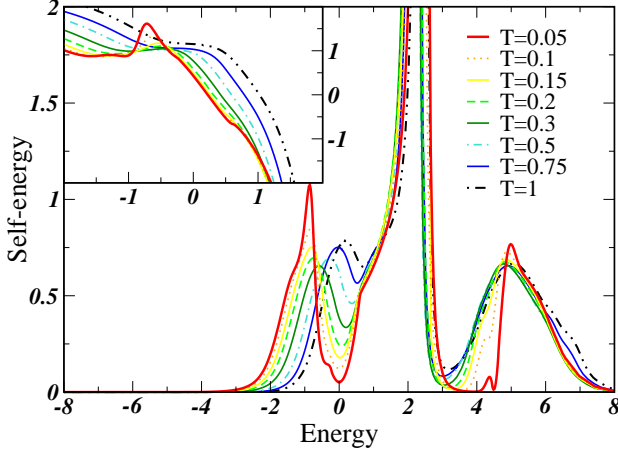


FIG. 20: Temperature dependence of imaginary part of the self-energy for $n = 0.8$. In the inset real part of the self-energy is shown for the same temperatures. Energy is in units of half bandwidth, D .

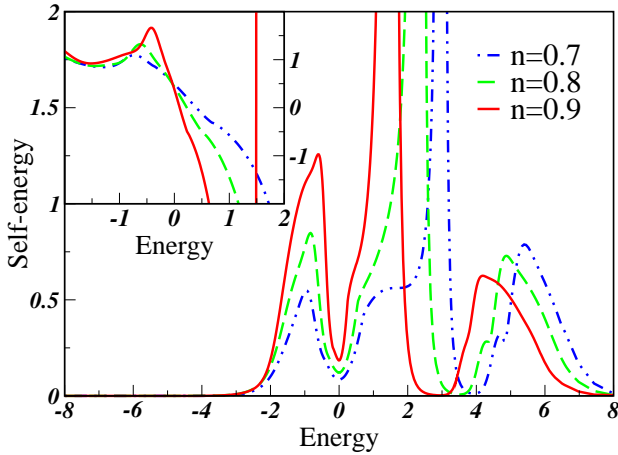


FIG. 21: Doping dependence of imaginary part of the self-energy for $T = 0.1$. In the inset real part of the self-energy is shown for the same dopings. Energy is in units of half bandwidth, D .

In Figs. 22 and 23 we plot temperature and density dependencies of the transport function for the same set of parameters as we used for Figs. 20 and 21, correspondingly. One can reveal similar features as in density of states: in the transport function behaviour one clearly identifies contributions coming from the upper Hubbard

band and lower one plus the QP peak. But the most important contribution to transport properties at low temperatures comes from energy region around the Fermi level. As it can be seen from Eqs. (55) the transport coefficients are entirely defined by the transport function integral in an energy window which depends on temperature. These equations allow at least qualitatively to define at least sign of the thermopower for all temperatures. If the slope of transport function is uprising then the thermopower should be negative and for the other slope it should be positive. For large energy window the sign of the thermopower will strongly depend on shape and position to the chemical potential of the transport function.

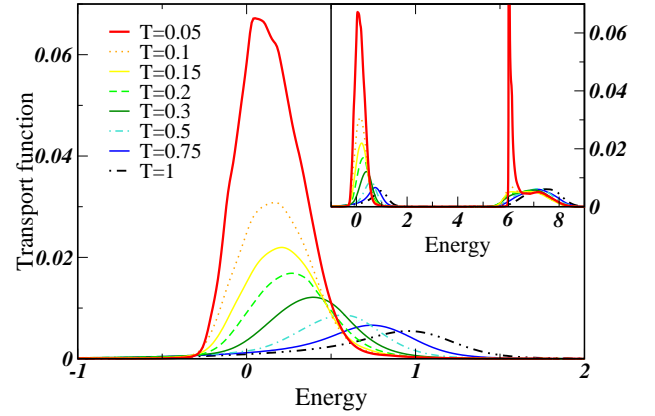


FIG. 22: Temperature dependence of the transport function for $n = 0.8$. In the inset larger frequency interval is used. Energy is in units of half bandwidth, D .

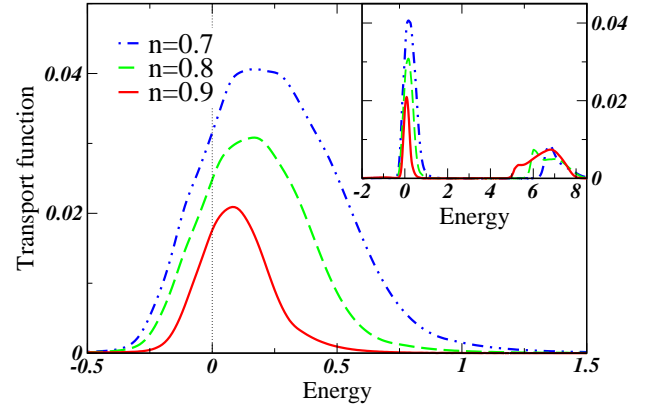


FIG. 23: Doping dependence of the transport function for temperature $T = 0.1$. In the inset larger frequency interval is shown. Energy is in units of half bandwidth, D .

B. Transport parameters

In Fig. 24 we plotted the transport parameters of the studied system for different densities against tempera-

ture. The transport parameters under consideration are the following: ρ denotes the electrical resistivity, κ is the thermal conductivity, S is the thermopower and L is the Lorentz ratio. The resistivity behaviour, as it was found experimentally⁴⁸ and theoretically, is a quadratic function at relatively low temperature interval becoming linear at higher temperatures (see Fig. 25). The quadratic temperature dependence of the electrical resistivity is reminiscent of the strong electron-electron scattering which predominates the electron-phonon scattering process. The thermal conductivity behaves as T^2 till temperatures of order 10^3 – 10^4 , which are relatively large temperatures⁵⁵. The Lorentz number tends to constant value around 16 – 17 $\text{nW}/\Omega/\text{K}^2$ indicating the character of the low temperature scattering as Fermi-liquid one. The thermopower behaviour is a bit more complicated. At low temperature the thermopower linearly tends to zero. It is very hard for us to distinguish doping dependence for relatively small temperatures as all changes lay between error bars which are in our case larger than the difference between lower and higher thermopower curves presented in the figure. The reason for large errors lays in a very small value of imaginary part of the self-energy which we have to deal with lowering the temperature and this situation is very challenging for the used impurity solvers. For higher temperatures (higher than 1000 K) we are certain in the thermopower behaviour as there is no any problems with the self-energy determination in this temperature range. With increasing temperature we observe a local maximum in the temperature interval 5×10^3 – 2×10^4 . We associate it with increasing the temperature cut-off (see Eq. (55)) which is large enough to take into account right-hand side slope of the central part in the transport function. Or in other words the local maximum in the thermopower in some way mimics behaviour of the transport function (the hump around the chemical potential).

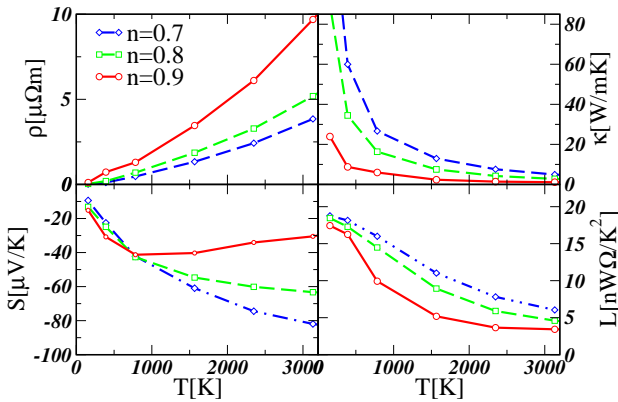


FIG. 24: Temperature and doping dependencies of transport parameters: ρ denotes the electrical resistivity, κ is the thermal conductivity, S is the thermopower and L is the Lorentz ratio.

Analyzing Figs. 24 and 25 as functions of doping for a fixed temperature we can see that all curves behave in the

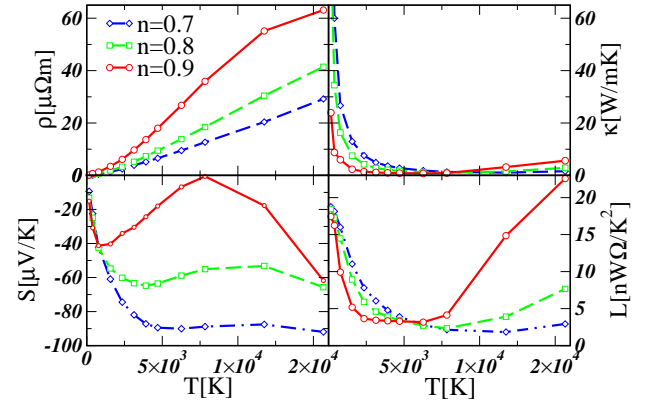


FIG. 25: The same transport parameters the same as in Fig. 24 but on substantially larger temperature interval.

way one would expect. The resistivity is growing with decreasing doping as the system approaches the MIT while the thermal conductivity and the Lorentz number are decreasing. The thermopower has a bit more complicated behaviour which depends on fixed temperature (which temperature slice we take). But generally it is growing with vanishing doping and for lower than 10% doping one could get even positive thermopower which first becomes positive at temperatures around 5000 K (see $n = 0.9$ thermopower curve) and then positiveness will propagate to smaller temperatures. Comparing our results with experimental situation in doped LaTiO_3 ^{43,59} we notice that majority of experiments are done for temperature less than 300 K which is a rather hard task to deal with for the reason we pointed out above. The biggest discrepancy we found for resistivity at small temperatures where our resistivity 3–4 times lower than the experimental one. While the thermopower behaviour (which we also treat as electronic one) is accurate within 30% in absolute value. One would expect that the thermopower could become positive with decreasing doping in the way it is experimentally observed. We also could obtain it once we do a much more delicate and hard job taking into account the structural transition happening at doping $x < 0.05$ as effectively we should have one-band model instead of three-fold degenerate. But this is beyond of the scope of the present work. Close to the MIT we have strongly asymmetric DOS and transport functions which in the case of integer filling $n = 1$ will produce positive sign of the thermopower. The reason for this is the position of negative slope (right-hand side) of the lower Hubbard band which is closer to the Fermi energy than the upper one and hence has dominant contribution into the transport properties of the system.

So, it would be fair to say that our calculations we can catch at least semi-qualitative behaviour of the transport parameters. The electrical resistivity would require an additional treatment to get quantitatively a good agreement while the thermopower calculations deserve quantitative comparison with experiment and can be accurate

enough providing 20-30 % agreement with experiment.

V II. C O N C L U S I O N

In the paper we proposed and implemented a new method for calculation of thermoelectrical properties in real materials. Dynamical mean-field theory was used to take into account strong electron interactions and thereby bring the self-energy into first-principles calculations. Taking a rather generic form for many strongly correlated materials density of states, we obtained temperature and doping dependencies for such thermoelectric properties as electrical resistivity, the thermal conductivity, the thermopower and the Lorentz ratio.

We believe that the new method will be a powerful tool for the analysis of existing experimental data and guiding us to a proper physical understanding of thermoelectrical phenomena. This is especially important not only for correlated materials such as Mott-Hubbard insulators and high-temperature superconductors but also for simple materials like the noble metals which display thermoelectric behavior that still lacks a proper description. In addition we hope this new method will aid in the search for new materials with better thermoelectrical performance by allowing for *ab initio* predictions of thermoelectric properties.

A c k n o w l e d g m e n t s

We would like to thank A. Lichtenstein for many fruitful and stimulation discussions. We greatly acknowledge usage of Cray T3E-900 computer at NERSC, Berkeley, as well as Rutgers Beowulf computational cluster which allowed us to make present computations feasible.

A P P E N D I X A : M A N Y B O D Y T H E O R Y I N A N O N - O R T H O G O N A L B A S I S

Our starting point here is a representation of the kinetic term of the Hamiltonian in an orthogonal basis, f_{ji} and we assume that this basis is related to the non-orthogonal basis, f_{ij} by the transformation matrix

$$f_{ji} = \sum_i f_{ij} S_i \quad \text{and} \quad h_{ij} = \sum_i h_{ji} S_i = \sum_i S_i^\dagger h_{ji} \quad (\text{A } 1)$$

The Hamiltonian is now given by

$$H = \sum_{ij} h_{ij} f_{ji}^\dagger c_j = \sum_{ij} S_i^\dagger h_{ji} f_{ij}^\dagger c_j = \sum_{ij} H_{ij} c_i^\dagger c_j \quad (\text{A } 2)$$

The last term in the equation above is a requirement that we place on the creation and destruction operators in the

non-orthogonal basis and thus we find that

$$c_i^\dagger = \sum_j c_j^\dagger S_{ji}^\dagger \quad \text{and} \quad c_i = \sum_j S_{ji} c_j \quad (\text{A } 3)$$

The non-orthogonality of the basis is encoded in the overlap matrix, $O = h_{ji}$ and this matrix can be related to the transformation matrix, S in the following manner

$$O_{ij} = h_{ji} = \sum_i S_i^\dagger h_{ji} S_j = \sum_i S_i^\dagger O_{ji} S_j \quad (\text{A } 4)$$

Therefore we see that the overlap matrix is given by

$$O = (S S^\dagger)^{-1} \quad (\text{A } 5)$$

We should note here that the creation operator c^\dagger does not create a particle in the state j when acting on the vacuum, since as we see

$$\begin{aligned} c^\dagger |j\rangle &= \sum_i c_i^\dagger S_{ji}^\dagger |j\rangle = \sum_i |j\rangle S_{ji}^\dagger \\ &= \sum_i |j\rangle S_{ji}^\dagger S_i^\dagger = \sum_i |j\rangle O^{-1} \end{aligned} \quad (\text{A } 6)$$

It is however worth noting that this state has unit overlap with the state j and zero overlap with all of the other basis-states! The commutation relationship of these operators are the same as for regular Fermi operators except that we get

$$f c_i^\dagger ; c_j = \sum_{ij} S_{ji} f c_i^\dagger ; c_j S_{ji}^\dagger = S_{ji} S_{ji}^\dagger = O^{-1} \quad (\text{A } 7)$$

Let us finally obtain the expression for the Green's function in the non-orthogonal basis

$$G(i) = \langle h c(i)^\dagger(0) i \rangle \quad (\text{A } 8)$$

The easiest way to calculate this Green's function is by looking at the Lagrangian for the system in the orthogonal basis and then simply transform it into the non-orthogonal one. We have (summation over repeated indices implied)

$$\begin{aligned} L &= c_i^\dagger \frac{\partial}{\partial} c_i - c_i^\dagger H_{ij} c_j \\ &= S_i^{-1} c_i^\dagger \frac{\partial}{\partial} c (S^\dagger)_i^{-1} - c^\dagger H c \\ &= c^\dagger O \frac{\partial}{\partial} c - c^\dagger H c \end{aligned} \quad (\text{A } 9)$$

The free Matsubara Green's function can now be obtained by Fourier transforming the operators in the Lagrangian and then the inverse of the Green's function, $G^0(i!)$, is simply the term multiplying $c^\dagger c$. Thus we obtain

$$G^0(i!) = [i! O^{-1} H]^{-1} \quad (\text{A } 10)$$

where L is a number of time slices. In addition to $L + 1$ $M_0; \dots; M_n, n = 0; \dots; L$, unknowns d_0 and d_n also should be provided. Last two unknowns entirely depend on the boundary conditions which we have to specify in order to have a unique solution of Eq. (C2). If one knows the first derivatives at the end-points then d_0 and d_n are defined through

$$d_0 = 1; d_0 = \frac{6}{h} \frac{G_1 - G_0}{h} - G_0^0; \\ d_n = 1; d_n = \frac{6}{h} G_n^0 - \frac{G_n - G_{n-1}}{h};$$

and $d_i = \frac{3}{h} \frac{G_{i+1} - G_i}{h} - \frac{G_i - G_{i-1}}{h}; i = 1; \dots; L-1$; for $i = 2; \dots; L-1$: More detailed derivations of the above formulae one can find in Ref. 60.

We can reduce number of unknowns just putting M_0 and M_n to zero (it is so called natural spline boundary conditions). In this case

$$d_0 = 0; d_0 = 0; d_n = 0; d_n = 0;$$

and we have the number of unknowns matching the number of equations, $L + 1$.

This boundary condition is good enough to compute FT of GF in the system at or close to half filling since the second derivative of the Green's function is small in absolute value in this regime. And using the natural spline boundary condition we do not impose a noticeable error. However, away from half filling when the asymmetry of the system grows, along with amplitude, of one out of the two second derivatives, usage of the natural spline eventually leads to pathological behavior of the self-energy. The signature of this pathology is in the "overshooting" effect⁶¹ when the self-energy at some finite Matsubara frequency i.e. the imaginary part of the self-energy, becomes positive in some frequency region on the positive Matsubara half-axis while it should be always negative. This, of course, amounts to having negative spectral weight for the self-energy which is something that does not occur for fermionic response functions. The "overshooting" can get especially severe in the limiting cases of small temperatures, small particle densities or large interaction strength.

So, to avoid the problem with the self-energy and, hence, with the whole procedure of the self-consistency in DMFT-QMC program we need to use the proper boundary conditions. And in this case we have two possibilities to get unique solution for the system of Eq. (C2) exploiting physical properties of studied GF: a) we can provide the first derivatives at both ends separately (in the next section we show how to calculate those derivatives) or b) we can provide the sum of the first and the sum of the second derivatives at the end-points, so called the first and the second moments of GF.

With the second choice of the boundary conditions (b) the system of equations becomes three-diagonal one with

two off-diagonal elements in the opposite corners of the matrix (M_{n-1} and $\frac{1}{2}M_0$)

$$\begin{aligned} 4M_0 + M_1 & & M_{n-1} & = d_0 \\ \frac{1}{2}M_0 + 2M_1 + \frac{1}{2}M_2 & & & = d_1 \\ \frac{1}{2}M_1 + 2M_2 + \frac{1}{2}M_3 & & & = d_2 \\ & \frac{1}{2}M_2 + 2M_3 + \frac{1}{2}M_4 & & = d_3 \\ & \ddots & \ddots & \vdots \\ \frac{1}{2}M_{n-3} + 2M_{n-2} + \frac{1}{2}M_{n-1} & & & = d_{n-2} \\ \frac{1}{2}M_0 & & \frac{1}{2}M_{n-2} + 2M_{n-1} & = d_{n-1} \end{aligned} \quad (C3)$$

where $d_0 = \frac{6}{h} \frac{G_1 - G_0}{h} + \frac{G_n - G_{n-1}}{h} M^{(1)} + 2M^{(2)}$, $d_{n-1} = \frac{6}{h} \frac{G_n + G_{n-2} - 2G_{n-1}}{h} - \frac{1}{2}B, G_0^0 + G_n^0 = M^{(1)}, M_0 + M_n = M^{(2)}$.

Now having the second derivatives M_i and, hence coefficients $a_i; b_i; c_i; d_i$ we can take Fourier integral analytically

$$\begin{aligned} G_m(i_n) &= \\ \frac{d}{dm} [a + b(\dots)_m + c(\dots)_m^2 + d(\dots)_m^3] e^{i(i_n)} &= \\ \frac{e^{i(i_n)} (6d + 2ic!_n + b!_n^2 - ia!_n^3)}{i_n^4} &= \\ \frac{1}{i_n^4} (e^{i(i_n)} (6d + 2ic!_n - 6i!_n d + b!_n^2 - 2c!_n^2 + & \\ 3(\dots)^2 d!_n^2 - ia!_n^3 + ib!_n^3 - ic(\dots)^2!_n^3 + i(\dots)^3 d!_n^3)) &= \end{aligned} \quad (C4)$$

Sum $G_m(i_n)$ over m

$$G(i_n) = \sum_{m=1}^{X^L} G_m(i_n);$$

will give us the Fourier integral in frequency space.

2. Inverse Fourier transformation

As it is well known Green's function $G(i_n)$ falls off as $1/i_n$ when $i_n \rightarrow 1$. In the program we deal with finite number of frequency points and cutting off $1/i_n$ tail one would make a rather crude approximation as the discontinuity of GF $G(i_n)$ (in imaginary time domain!) has been removed. In such situation, the high-frequency tail has to be extracted from $G(i_n)$ and Fourier transformed analytically using the following Fourier relation

$$\frac{1}{i_n!} \sim [(\dots) + n(\dots)] e^{i(i_n)}; \quad (C5)$$

where $n(i_n) = 1 = [\exp(-g)]$ and $g = 1$ depending on whether i_n is bosonic or fermionic.

The inverse Fourier transformation for GF without the tail is made by straightforward summation over Matsubara frequencies. Once it has been done we add the information about the tail using Eq. (C5).

APPENDIX D: MOMENTS

Moments, $M^{(k)}$, are nothing else as the expansion of GF in frequency domain

$$G(i!) = \sum_{k=0}^{\infty} \frac{M^{(k)}}{i^{k+1}}; \quad (D1)$$

Another definition of k -degree moment is the following

$$M^{(k)} = \frac{1}{d!} i^k (i!); \quad (D2)$$

where $(i!)$ is density of states (DOS).

Moments $M^{(k)}$ can be bind to sum of GFs and sum of its derivatives in imaginary-time space as

$$(i!)^{k+1} (G^{(k)}(0^+) + G^{(k)}(i)) = M^{(k)}; \quad (D3)$$

where $k = 0, \dots, N$.

To show this one needs to take Fourier integral in parts

$$\begin{aligned} G(i!) &= \int_0^Z e^{i!n} G(i) d \\ &= \sum_{k=0}^N \frac{(i!)^{k+1} (G^{(k)}(0^+) + G^{(k)}(i))}{(i!)^{k+1}} \\ &+ \frac{(i!)^{N+1}}{(i!)^{N+1}} \int_0^Z e^{i!n} \frac{\partial^{N+1} G(i)}{\partial^{N+1}} d; \end{aligned} \quad (D4)$$

So, to solve the system of Eq. (C3) we need to adhere to the proper boundary conditions which are expressed through the various moments of the Green's function. What we need really it to provide the first three moments $M^{(0)}, M^{(1)}, M^{(2)}$. The first moment for Green's function is equal to one, the second moment proportional to the chemical potential in the system and the third one is a little bit more complicated and contains a density-density correlator. To show that we start with the single impurity Anderson model which reads

$$\begin{aligned} H_{SIAM} &= \sum_k \epsilon_k c_k^\dagger c_k + \sum_k (\epsilon_k + \frac{1}{2} \sum_{\sigma} U_{\sigma}) f^\dagger f \\ &+ \sum_k V_k (f^\dagger c_k + c_k^\dagger f) \\ &+ \sum_{\sigma} \sum_{\sigma'} U_{\sigma} (n_{\sigma} - \frac{1}{2} (n_{\sigma} + n_{\sigma'})); \end{aligned} \quad (D5)$$

where $\epsilon_k = \epsilon_0 + \frac{1}{2} \sum_{\sigma} U_{\sigma}$, the first three moments be obtained from the following commutators

$$M^{(k)} = f L^k f; f^\dagger g_+;$$

where $L O = [O, H]$ denotes the commutator of operator O with the Hamiltonian, and $f \ddot{::} g_+$ is the anticommutator. After some algebra one finds the following expressions for the moments

$$M^{(0)} = f; f^\dagger = 1; \quad (D6)$$

$$M^{(1)} = [f; H]; f^\dagger = \epsilon_k + \sum_{\sigma} U_{\sigma} (n_{\sigma} - \frac{1}{2});$$

$$\begin{aligned} M^{(2)} &= \frac{1}{2} [[f; H]; H]; f^\dagger = \frac{1}{2} [f; H]; [H; f^\dagger] = \\ &= \epsilon_k^2 + 2\epsilon_k \sum_{\sigma} U_{\sigma} (n_{\sigma} - \frac{1}{2}) + \\ &+ \sum_{\sigma, \sigma'} \sum_k U_{\sigma} U_{\sigma'} (n_{\sigma} - \frac{1}{2}) (n_{\sigma'} - \frac{1}{2}) + \sum_k V_k^2; \end{aligned}$$

where $\sum_k V_k^2 = M_0^2 - (M_1^1)^2$, and the moments M_0^i are defined by Eq. (D2) with $(i!) = D(i!)$, $D(i!)$ is non-interacting DOS.

Summing up similar terms in $SU(N)$ approximation we get

$$M^{(1)} = \epsilon_k + (2N-1)U_n; \quad (D7)$$

$$\begin{aligned} M^{(2)} &= \epsilon_k^2 + 2\epsilon_k (2N-1)U_n + \\ &+ U^2 [(2N-1)n + \ln n] + \sum_k V_k^2; \end{aligned} \quad (D8)$$

where n is filling per band and per spin, $n = \frac{1}{P} \sum_{\sigma} n_{\sigma}$, and double occupancy is defined as $\ln n = \sum_{\sigma} \ln n_{\sigma}$.

The second way to make the correct cubic spline as we mentioned before in section C1 is to provide the first derivatives at both ends of imaginary time interval (the boundary conditions). To find the first derivatives at the ends one can use the following definition of the first derivatives of finite-temperature GF

$$\frac{\partial}{\partial T} T f(i) f^\dagger(0) = T [H; f] f^\dagger = G^0(0^+);$$

Using as the Hamiltonian $H = H_{SIAM}$ we can easily obtain the derivatives at the ends

$$\begin{aligned} G^0(0^+) &= \epsilon_k (1 - n_k) + \sum_k V_k c_k f^\dagger + \\ &+ \sum_k U_{\sigma} (n_{\sigma} - \ln n_{\sigma}); \\ G^0(i) &= \epsilon_k n_k + \sum_k V_k f^\dagger c_k + \\ &+ \sum_k U_{\sigma} \ln n_{\sigma}; \end{aligned} \quad (D9)$$

where averages e.g. $\sum_k V_k c_k f^\dagger$ can be calculated

$$\begin{aligned} \sum_k V_k c_k f^\dagger &= T \sum_n (i!)_n G(i!)_n; \end{aligned}$$

In obtained formulae (Eqs. (D 6)–(D 9)) we should know ϵ_n , n , for each band and spin as well as we should know density-density correlator χ_n . The thing we can extract from GF itself. Calculation of the correlator in QMC highlights one of the advantages of the method: the correlator is provided by the QMC itself and one does not need to rely on any additional approximations to obtain it as e.g. in the case of multiband IPT method⁶² where coherent potential approximation is used to get the correlator. At each time slice the density-density correlator is also computed from GF but in imaginary time domain where it is simply a product of two Green's functions in $(\tau; \omega)$ space. We should note here that we compute the correlator along with other parameters in the system at each iteration step and once the self-consistency is reached we have correctly obtained all the components and parameters in the system. And finally, with small enough imaginary time step one can completely avoid the "overshooting" problem. Keeping in mind the main limitation of QMC procedure $U = 2 < 1$.

In the present computations we choose $U = 1=4$ which is good enough for the range of parameters we use in the current paper.

APPENDIX E: SUNCA EQUATIONS

In this Appendix, we explicitly give the SUNCA equations for degenerate Anderson impurity model with $N=2$ bands considering fluctuations between states with $M=1$, M and $M+1$ electrons on the impurity. Self-energies are analytically continued to real frequencies and projected onto the physical $Q=1$ subspace. We first define the ladder vertex functions T_a, T_b with rungs of pseudo-particles a (with $M+1$ electrons) and b (with $M=1$ electrons), respectively, as shown diagrammatically in Fig. 4. These vertex functions, obey the following Bethe-Salpeter equations,

$$T_a(\omega; \tau) = 1 + (N - M) \int \frac{d\omega'}{2\pi} A_c^0(\omega - \omega') G_f(\omega') G_a(\omega + \omega') T_a(\omega'; \tau); \quad (E1)$$

$$T_b(\omega; \tau) = 1 + M \int \frac{d\omega'}{2\pi} A_c^0(\omega - \omega') G_f(\omega') G_b(\omega + \omega') T_b(\omega'; \tau); \quad (E2)$$

where $f(\omega)$ is the Fermi function and $A_c^0(\omega) = \frac{1}{\pi} \text{Im} G_c^0(\omega)$ is the bare conduction electron density of states. For concreteness, all propagators are to be understood as the retarded ones. The auxiliary particle self-energies (Fig. 3) are then given by,

$$\begin{aligned} \Sigma_f(\omega) = & M \int \frac{d\omega'}{2\pi} f(\omega') A_c^0(\omega - \omega') G_b(\omega') T_a(\omega'; \tau)^2 + (N - M) \int \frac{d\omega'}{2\pi} f(\omega') A_c^0(\omega - \omega') G_a(\omega') T_b(\omega'; \tau)^2 \\ & + 2M(N - M) \int \frac{d\omega'}{2\pi} f(\omega') A_c^0(\omega - \omega') G_b(\omega') \int \frac{d\omega''}{2\pi} f(\omega'') A_c^0(\omega' - \omega'') G_f(\omega'') G_a(\omega' + \omega''); \end{aligned} \quad (E3)$$

$$\begin{aligned} \Sigma_b(\omega) = & (N - M + 1) \int \frac{d\omega'}{2\pi} f(\omega') A_c^0(\omega - \omega') G_f(\omega') T_a(\omega'; \tau) + (N - M + 1)(N - M) \int \frac{d\omega'}{2\pi} f(\omega') A_c^0(\omega - \omega') G_f(\omega') \\ & \int \frac{d\omega''}{2\pi} f(\omega'') A_c^0(\omega' - \omega'') G_f(\omega'') G_a(\omega' + \omega'') [T_b(\omega'; \tau) T_b(\omega''; \tau) - 1]; \end{aligned} \quad (E4)$$

$$\begin{aligned} \Sigma_a(\omega) = & (M + 1) \int \frac{d\omega'}{2\pi} f(\omega') A_c^0(\omega - \omega') G_f(\omega') T_b(\omega'; \tau) + (M + 1)M \int \frac{d\omega'}{2\pi} f(\omega') A_c^0(\omega - \omega') G_f(\omega') \\ & \int \frac{d\omega''}{2\pi} f(\omega'') A_c^0(\omega' - \omega'') G_f(\omega'') G_b(\omega' + \omega'') [T_a(\omega'; \tau) T_a(\omega''; \tau) - 1]; \end{aligned} \quad (E5)$$

In order to calculate the local electron spectral function A_d from the self-consistently determined G_a, G_b, G_f , it is convenient to define modified vertex functions as

$$S_a^R(\omega; \tau) = 1 + (N - M) \int \frac{d\omega'}{2\pi} f(\omega') A_c^0(\omega - \omega') \text{Re} f G_f(\omega') T_a(\omega'; \tau) g G_a(\omega + \omega'); \quad (E6)$$

$$S_a^I(\omega; \tau) = (N - M) \int \frac{d\omega'}{2\pi} f(\omega') A_c^0(\omega - \omega') \text{Im} f G_f(\omega') T_a(\omega'; \tau) g G_a(\omega + \omega'); \quad (E7)$$

$$S_b^R(\omega; \tau) = 1 + M \int \frac{d\omega'}{2\pi} f(\omega') A_c^0(\omega - \omega') \text{Re} f G_f(\omega') T_b(\omega'; \tau) g G_b(\omega + \omega'); \quad (E8)$$

$$S_b^I(\omega; \tau) = M \int \frac{d\omega'}{2\pi} f(\omega') A_c^0(\omega - \omega') \text{Im} f G_f(\omega') T_b(\omega'; \tau) g G_b(\omega + \omega'); \quad (E9)$$

The local spectral function then reads

$$\begin{aligned}
 A_d(!) = & \sum_{M=1}^N \sum_{N=1}^M \int \frac{d!}{f(!)} \text{Im} \left[\frac{e}{2} G_f(+!) \text{Im} [G_b(!)] S_a^R(!;)^2 - S_a^I(!;)^2 \right] + 2 \text{Re} [G_b(!)] S_a^R(!;) S_a^I(!;) \\
 & \sum_{M=1}^N \sum_{N=1}^M \int \frac{d!}{f(!)} \text{Im} \left[\frac{e}{2} G_f(!) \text{Im} [G_a(!)] S_b^R(!;)^2 - S_b^I(!;)^2 \right] + 2 \text{Re} [G_a(!)] S_b^R(!;) S_b^I(!;) \\
 & + 2M \sum_{M=1}^N \sum_{N=1}^M \int \frac{d!}{f(!)} \int \frac{d!}{f(!)} A_C^0(!) \text{Im} [G_b(!) G_f(!)] \text{Im} [G_f(+!) G_a(+!)]; \quad (\text{E10})
 \end{aligned}$$

Note that the exponential divergencies of the statistical factors appearing in Eq. (E10) are compensated by the threshold behavior of the corresponding auxiliary particle spectral functions $A_d(!) = \frac{1}{2} \text{Im} G_d(!)$, $d = a, b, f$ in the integrands. For the numerical treatment, these divergencies can be explicitly absorbed by formulating the self-consistency equations (A1)-(A10) in terms of the functions $\tilde{A}_d(!)$ which are defined via

$$A_d(!) = f(!) \tilde{A}_d(!); \quad (\text{E11})$$

and, hence, have no exponential divergence. We thus have, e.g., $\exp(-!) A_d(!) = f(!) \tilde{A}_d(!)$.

APPENDIX F: TRANSPORT CALCULATIONS: CURRENTS DERIVATION

Below we derive the expressions for the currents in a general basis. This is done by extending the gauge-theoretic method developed in Ref. 63. In the non-orthogonal basis the action for the system can be expressed as follows

$$S = \sum_k \int d\tau \sum_{\alpha} c_k^{\dagger} O_k \left[\frac{\delta}{\delta \tilde{A}_p} + H_k \right] c_k; \quad (\text{F1})$$

Here $\frac{\delta}{\delta \tilde{A}_p} = \frac{1}{2} (\frac{\delta}{\delta \tilde{A}_p} - \frac{\delta}{\delta \tilde{A}_p})$ denotes the anti-symmetrized time derivative. The particle and heat currents can now be obtained by considering the invariance of the action under local phase transformation and local translations in time respectively. In the orthogonal case one is lead to the following expression for the currents

$$\mathcal{J} = \frac{\partial H[\tilde{A}_p]}{\partial \tilde{A}_p} \Big|_{\tilde{A}_p=0} \quad \text{and} \quad \mathcal{Q} = \frac{\partial H[\tilde{A}_h]}{\partial \tilde{A}_h} \Big|_{\tilde{A}_h=0}; \quad (\text{F2})$$

where \tilde{A}_p and \tilde{A}_h are gauge fields conjugate to the currents and $H[\tilde{A}_p]$ and $H[\tilde{A}_h]$ denote the gauged Hamiltonian, i.e. the Hamiltonian with the replacements $\tilde{K} \rightarrow \tilde{K} + \tilde{A}_h$ respectively. This replacement is performed in both the kinetic and the interaction terms but not in the field operators. In our case however the overlap matrix appearing in the action depends also on momentum and therefore the proper generalization of the currents to non-orthogonal basis will also take the overlap matrix into account. Thus we obtain

$$\mathcal{J} = \frac{\partial (O[\tilde{A}_p] \frac{\delta}{\delta \tilde{A}_p} + H[\tilde{A}_p])}{\partial \tilde{A}_p} \Big|_{\tilde{A}_p=0}; \quad (\text{F3})$$

$$\mathcal{Q} = \frac{\partial (O[\tilde{A}_h] \frac{\delta}{\delta \tilde{A}_h} + H[\tilde{A}_h])}{\partial \tilde{A}_h} \Big|_{\tilde{A}_h=0}; \quad (\text{F4})$$

Performing these operations leads to the following expressions

$$\mathcal{J} = \sum_k \mathbf{v}_k; B_k^{(0)} - \mathbf{u}_k; B_k^{(1)}; \quad (\text{F5})$$

$$\mathcal{Q} = \sum_k \mathbf{v}_k; B_k^{(1)} - \mathbf{u}_k; B_k^{(2)}; \quad (\text{F6})$$

where we have defined

$$B_k^{(n)} = (-1)^n c_k^{\dagger} \left(\frac{\delta}{\delta \tilde{A}_p} \right)^n c_k; \quad (\text{F7})$$

and

$$\mathbf{v}_k; = \frac{1}{h} \tilde{\mathbf{r}}_k H_k^0, \quad \text{and} \quad \mathbf{u}_k; = \frac{1}{h} \tilde{\mathbf{r}}_k O_k; \quad (\text{F8})$$

where H_k^0 is the tight-binding, LMTO Hamiltonian of the system and O_k is the overlap matrix that captures the non-orthogonality of the basis that we are using. The validity of the expressions above is not restricted to DMFT and they are in fact true for all density-density interactions such as the Hubbard interaction. This is because the interaction terms are gauge invariant and therefore they do not contribute to the expressions for the currents.

- ¹ A. Georges, G. Kotliar, W. Krauth, and M. J. Rozenberg, *Rev. Mod. Phys.* **68**, 13 (1996).
- ² G. Kotliar, *Eur. Phys. J. B* **11**, 27 (1999).
- ³ V. I. Anisimov et al., *J. Phys. C* **9**, 7359 (1997).
- ⁴ A. I. Lichtenstein and M. I. Katsnelson, *Phys. Rev. B* **57**, 6884 (1998).
- ⁵ *Theory of the Inhomogeneous Electron Gas*, edited by S. Lundqvist and S. H. March (Plenum, New York, 1983).
- ⁶ F. Aryasetiawan and O. Gunnarsson, *Rep. Prog. Phys.* **61**, 237 (1998).
- ⁷ V. I. Anisimov, J. Zaanen, and O. K. Andersen, *Phys. Rev. B* **44**, 943 (1991).
- ⁸ I. Yang, S. Y. Savrasov, and G. Kotliar, *Electronic Archive*, xxx.janlgov, cond-mat/0107063 (2001).
- ⁹ G. Kotliar and S. Savrasov, in *New Theoretical approaches to strongly correlated systems*, edited by A. M. Tsvelik (Kluwer Academic Publishers, The Netherlands, 2001).
- ¹⁰ J. E. Hirsch and R. M. Fye, *Phys. Rev. Lett.* **56**, 2521 (1986).
- ¹¹ K. Haule, S. K. Kirchner, J. Kroha, and P. W. Lee, *Phys. Rev. B* **64**, 155111/7 (2001).
- ¹² I. A. Nekrasov et al., *Euro Phys. J. B* **18**, 133 (2000).
- ¹³ K. Held et al., *Int. J. Mod. Phys. B* **15**, 2611 (2001).
- ¹⁴ D. van der Marel and G. A. Sawatzky, *Phys. Rev. B* **37**, 10674 (1988).
- ¹⁵ A. K. M. M. Rahman, R. M. Martin, and S. Satpathy, *Phys. Rev. B* **38**, 6650 (1988).
- ¹⁶ M. S. Hybertsen, M. Schluter, and N. E. Christensen, *Phys. Rev. B* **39**, 9028 (1989).
- ¹⁷ J. F. Annett, R. M. Martin, A. K. M. Rahman, and S. Satpathy, *Phys. Rev. B* **40**, 2620 (1989).
- ¹⁸ O. Gunnarsson, *Phys. Rev. B* **41**, 514 (1990).
- ¹⁹ J. Zaanen and G. A. Sawatzky, *J. Solid State Chem.* **88**, 8 (1990).
- ²⁰ V. I. Anisimov and O. Gunnarsson, *Phys. Rev. B* **43**, 7570 (1991).
- ²¹ O. K. Andersen, *Phys. Rev. B* **12**, 3060 (1975).
- ²² V. I. Anisimov, F. Aryasetiawan, and A. I. Lichtenstein, *J. Phys.: Condens. Matter* **9**, 767808 (1997).
- ²³ I. Paul and G. Kotliar, *Electronic Archive*, xxx.janlgov, cond-mat/0211538 (2002).
- ²⁴ O. K. Andersen and T. Saha-Dasgupta, *Phys. Rev. B* **62**, R16219 (2000).
- ²⁵ J. E. Hirsch, *Phys. Rev. B* **28**, 4059-4061 (1983).
- ²⁶ K. Takegahara, *J. Phys. Soc. Jpn.* **62**, 1736 (1992).
- ²⁷ A. A. Abrikosov, *Physics* **2**, 21 (1965).
- ²⁸ T. A. Costi, P. Schmitteckert, J. Kroha, and P. W. Lee, *Phys. Rev. Lett.* **73**, 1275-1278 (1994).
- ²⁹ J. Kroha and P. W. Lee, in *Theoretical Methods for Strongly Correlated Electrons*, CRM Series in Mathematical Physics, edited by C. B. D. Senechal, A. M. Tremblay (Springer, New York, 2003).
- ³⁰ M. Jarrell and J. E. Gubernatis, *Physics Reports* **269**, 133 (1996).
- ³¹ G. D. Mahan, *Many-Particle Physics*, 2nd ed. (Plenum, New York, N.Y., 1993).
- ³² E. I. Blount, *Solid State Physics* **13**, 305 (1962).
- ³³ A. J. Millis, *J. Electron Spectroscopy and Related Phenomena* **114-116**, 669 (2001).
- ³⁴ P. Lambin and J. P. Vigneron, *Phys. Rev. B* **29**, 3430 (1984).
- ³⁵ D. J. Singh and I. I. Mazin, *Phys. Rev. B* **56**, R1650 (1997).
- ³⁶ S. G. Kim, I. I. Mazin, and D. J. Singh, *Phys. Rev. B* **57**, 6199 (1998).
- ³⁷ M. Fomari and D. J. Singh, *Electronic Archive*, xxx.janlgov, cond-mat/9904307 (1999).
- ³⁸ J. E. Sunstrom, IV, S. M. Kauzlarich, and P. Klavins, *Chem. Mater.* **4**, 346 (1992).
- ³⁹ Y. Maeno, S. A. Awaj, H. M. Atsumoto, and T. Fujita, *Physica B* **165-166**, 1185 (1990).
- ⁴⁰ D. A. Crandles, T. Timusk, J. D. Garrett, and J. E. Greedan, *Physica C* **201**, 407 (1992).
- ⁴¹ M. Onoda and M. Yasumoto, *J. Phys.: Condens. Matter* **9**, 3861 (1997).
- ⁴² M. Onoda and M. Kohno, *J. Phys.: Condens. Matter* **10**, 1003 (1998).
- ⁴³ C. C. Hays, J. S. Zhou, J. T. Markert, and J. B. Goodenough, *Phys. Rev. B* **60**, 10367 (1999).
- ⁴⁴ E. Pavarini et al., *Electronic Archive*, xxx.janlgov, cond-mat/0309102 (2003).
- ⁴⁵ J. B. Goodenough, *Prog. Solid State Chem.* **5**, 145 (1971).
- ⁴⁶ K. Kumagai et al., *Phys. Rev. B* **48**, 76367642 (1993).
- ⁴⁷ Y. Okada et al., *Phys. Rev. B* **48**, 96779683 (1993).
- ⁴⁸ Y. Tokura et al., *Phys. Rev. Lett.* **70**, 2126 (1993).
- ⁴⁹ S. A. Carter et al., *Phys. Rev. B* **48**, 16841 (1993).
- ⁵⁰ M. J. Rozenberg, G. Kotliar, and X. Y. Zhang, *Phys. Rev. B* **49**, 10181 (1994).
- ⁵¹ M. Rozenberg et al., *Phys. Rev. Lett.* **75**, 105 (1995).
- ⁵² G. Kotliar and H. Kajueter, *Phys. Rev. B* **54**, 14221 (1996).
- ⁵³ H. Kajueter, G. Kotliar, and G. Müller, *Phys. Rev. B* **53**, 16214 (1996).
- ⁵⁴ H. Kajueter and G. Kotliar, *Int. J. Mod. Phys. B* **11**, 729 (1997).
- ⁵⁵ G. Palsson and G. Kotliar, *Phys. Rev. Lett.* **80**, 4775 (1998).
- ⁵⁶ D. D. Sama, S. R. Barman, H. Kajueter, and G. Kotliar, *Europhys. Lett.* **36**, 307 (1996).
- ⁵⁷ I. Solovyev, N. Hamada, and K. Terakura, *Phys. Rev. B* **53**, 7158 (1996).
- ⁵⁸ H. Kajueter and G. Kotliar, *Phys. Rev. Lett.* **77**, 131 (1996).
- ⁵⁹ R. Moos, A. Gnudi, and K. H. Hardtl, *J. Appl. Phys.* **78**, 5042 (1995).
- ⁶⁰ J. Stoer and R. Bulirsch, *Introduction to Numerical Analysis* (Springer-Verlag, New York Berlin Heidelberg, 1980).
- ⁶¹ V. S. Odovenko and G. Kotliar, *Phys. Rev. B* **65**, 075102 (2002).
- ⁶² H. Kajueter, Ph.D. thesis, Rutgers University, Graduate School New Brunswick, NJ, 1996.
- ⁶³ J. Moreno and P. Coleman, *Electronic Archive*, xxx.janlgov, cond-mat/9603079 (1996).